

# **Solid-State Lifshitz-van der Waals Repulsion through Two-Dimensional Materials**

Tian Tian<sup>1</sup>, Franzisca Naef<sup>1</sup>, Gianluca Vagli<sup>1</sup>, Kemal Celebi<sup>1</sup>, Yen-Ting Li<sup>2, 3</sup>,  
Shu-Wei Chang<sup>2</sup>, Frank Krumeich<sup>4</sup>, Elton J. G. Santos<sup>5</sup>, Yu-Cheng Chiu<sup>2</sup>, and  
Chih-Jen Shih <sup>\*1</sup>

<sup>1</sup>Institute for Chemical and Bioengineering, ETH Zürich, CH-8093 Zürich,  
Switzerland

<sup>2</sup>Department of Chemical Engineering, National Taiwan University of Science  
and Technology, Taipei 10607, Taiwan

<sup>3</sup>National Synchrotron Radiation Research Center, Hsinchu 30076, Taiwan

<sup>4</sup>Laboratory of Inorganic Chemistry, ETH Zürich, 8093, Zürich, Switzerland

<sup>5</sup>Institute for Condensed Matter Physics and Complex Systems, School of Physics  
and Astronomy, The University of Edinburgh, EH9 3FD, UK.

---

\*Correspondence to C.-J.S. [chih-jen.shih@chem.ethz.ch](mailto:chih-jen.shih@chem.ethz.ch)

The van der Waals (vdW) force is a ubiquitous short-range interaction between atoms and molecules<sup>1,2</sup> that underlies many fundamental phenomena<sup>3-5</sup>. Early pairwise additive theories pioneered by Keesom<sup>6</sup>, Debye<sup>7</sup>, and London<sup>8</sup> suggested the force to be monotonically attractive for separations larger than the vdW contact distance. However, seminal work by Lifshitz et al.<sup>9</sup> predicted that quantum fluctuations can change the sign of vdW interactions from attractive to repulsive. Although recent experiments carried out in fluid environment have demonstrated the long-range counterpart – the Casimir repulsion<sup>10-12</sup>, it remains controversial whether the vdW repulsion exists<sup>13-15</sup>, or is sufficiently strong to alter solid-state properties. Here we show that the atomic thickness and birefringent nature of two-dimensional (2D) materials, arising from their anisotropic dielectric responses, make them a versatile medium to tailor the many-body Lifshitz-vdW interactions at solid-state interfaces. Based on our theoretical prediction, we experimentally examine two heterointerface systems in which the vdW repulsion becomes comparable to the two-body attraction. We demonstrate that the in-plane movement of gold atoms on a sheet of freestanding graphene becomes nearly frictionless at room temperature. Repulsion between molecular solid and gold across graphene results in a new polymorph with enlarged out-of-plane lattice spacings. The possibility of creating repulsive energy barriers in nanoscale proximity to an uncharged solid surface offers technological opportunities such as single-molecule actuation and atomic assembly.

When two electroneutral objects, A and B, are brought in proximity in a polarizable medium, m, the correlations in their temporal electromagnetic (EM) fluctuations usually lead to an attractive interaction<sup>3</sup>. At small separations (< 10 nm), this is the vdW force<sup>1</sup>, and at large separations (> 20 nm) known as the Casimir force<sup>10,11</sup>. The existence of Casimir repulsion was theoretically predicted via the manipulation of EM modes at the interacting surfaces<sup>16-19</sup>, which was later experimentally measured<sup>12,20-22</sup>. As the interaction potential in the Lifshitz theory<sup>1,9</sup> is proportional to the product of effective polarizabilities of A and B screened by m, the most straightforward approach to generate Casimir or vdW repulsion is to design a set of materials such that<sup>12</sup>

$$(\epsilon_A - \epsilon_m)(\epsilon_B - \epsilon_m) < 0 \quad (1)$$

where  $\epsilon_A$ ,  $\epsilon_B$ ,  $\epsilon_m$  are the frequency-dependent dielectric responses for A, B, and m, respectively. Accordingly, the experiments demonstrating long-range Casimir repulsion were majorly carried out in high-refractive-index fluids, i.e., m=fluid, in which  $\epsilon_m$  is between  $\epsilon_A$  and  $\epsilon_B$  over a wide range of frequencies to

obey inequality (1).

However, the examination of vdW repulsion in a fluid<sup>13–15,23,24</sup>, has two fundamental limitations. First, the high-refractive-index fluid medium is made by highly polar molecules, and their orientation and polarity within the small separating gap may disturb the force<sup>12</sup>. Second, more critically, the fluid dielectric response usually drops rapidly beyond the visible frequency region, lowering  $\epsilon_m$  below  $\epsilon_A$  and  $\epsilon_B$ <sup>25</sup> that results in high-frequency attraction. The long-range repulsive force observed in fluid arises from the retardation of the high-frequency contributions, but when working at small separations, the full-spectrum summation may convert the force from repulsion to attraction<sup>25</sup>. The existence of vdW repulsion thus remains elusive.

In principle, there is no reason why vdW repulsion cannot exist in solid-state systems. The inequality (1) can be easily fulfilled, for example, by placing an ultrathin semiconductor sandwiched between a metal and an insulator. The major challenge is to properly design a set of materials where the vdW repulsion is sufficiently strong to be observed. In this work, we prove that the Lifshitz formalism remains valid in the vdW regime, successfully predicting the existence of vdW repulsion in the 2D materials-mediated systems.

The idea of investigating the 2D materials-mediated repulsive vdW forces was inspired by recent findings of the wetting transparency<sup>26–30</sup> and the remote epitaxy<sup>31,32</sup> on graphene-coated substrates. In these systems, the vdW interactions exerted by the substrate (A) can be transmitted through the monolayer-containing medium (m) and greatly influence the thermodynamic properties on the other side (B), meaning that 2D materials are highly transparent to vdW interactions. We therefore predict, if the dielectric response of the 2D material medium is between  $\epsilon_A$  and  $\epsilon_B$ , a strong vdW repulsion may be generated.

Consider two semi-infinite bulk materials A and B separated by a gap containing a sheet of monolayer 2D material (Fig. 1a). When the separation  $d$  is larger than the vdW thickness of monolayer, we treat the separating gap containing the monolayer surrounded by vacuum as an effective birefringent medium with distinct in-plane (IP) and out-of-plane (OP) dielectric responses  $\epsilon_m^{\parallel}$  and  $\epsilon_m^{\perp}$ , which are functions of  $d$  and imaginary frequency  $i\xi$ , respectively, resulted from the different IP and OP electronic properties of the monolayer. Using the polarizability theory of 2D materials<sup>33</sup>,  $\epsilon_m^{\parallel}$  and  $\epsilon_m^{\perp}$  are given by  $\epsilon_m^{\parallel}(d) = 1 + \frac{\alpha_{2D}^{\parallel}}{\epsilon_0 d}$  and  $\epsilon_m^{\perp}(d) = \left(1 - \frac{\alpha_{2D}^{\perp}}{\epsilon_0 d}\right)^{-1}$ , where  $\alpha_{2D}^{\parallel}$  and  $\alpha_{2D}^{\perp}$  are the  $d$ -independent IP and OP polarizabilities for the 2D material extracted from first principle calculations, respectively (for details see *Methods*).

The vdW interaction potential between A and B across a birefringent medium m,  $\Phi_{AmB}^{\text{vdW}}$ , is given by<sup>1</sup> (for

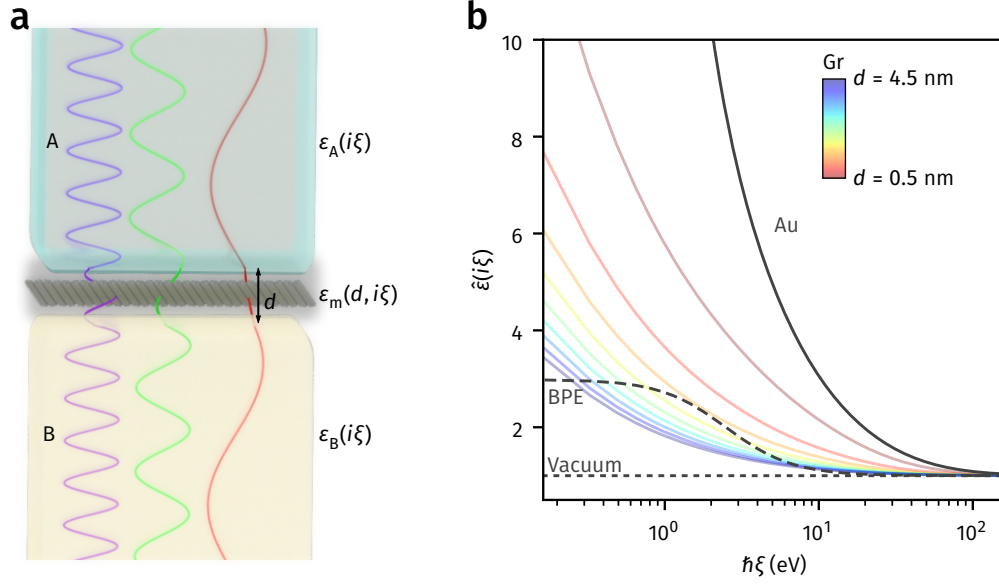


Figure 1: **vdW repulsion in 2D materials-mediated systems.** **a.** The interaction potential between material A and material B across a birefringent medium gap  $m$  containing a sheet of monolayer 2D material becomes repulsive when  $[\epsilon_A(i\xi) - \hat{\epsilon}_m(d, i\xi)][\epsilon_B(i\xi) - \hat{\epsilon}_m(d, i\xi)] < 0$  at given imaginary frequency  $i\xi$  and separation  $d$ . **b.** Dielectric responses for Au, BPE, Vac, and Gr at different separations as a function of electromagnetic energy,  $\hbar\xi$ , for different separations. Accordingly, vdW repulsion may be observed in two sets of materials,  $A/m/B = \text{Vac/Gr/Au}$  and  $\text{Au/Gr/BPE}$ .

details see *Methods*):

$$\Phi_{\text{AmB}}^{\text{vdW}}(d) = \sum_{n=-\infty}^{\infty} G_{\text{AmB}}(i\xi_n) = \sum_{n=-\infty}^{\infty} \frac{k_B T g_m(i\xi_n)}{16\pi d^2} \left\{ \int_n^{\infty} q \ln [1 - \Delta_{\text{Am}}(i\xi_n) \Delta_{\text{Bm}}(i\xi_n) e^{-q}] d \right\} \quad (2)$$

where  $k_B$  is the Boltzmann constant,  $T$  is the absolute temperature,  $\xi_n = 2\pi n k_B T / \hbar$  is the  $n$ -th Matsubara frequency,  $\hbar$  is the reduced Planck constant,  $r_n = \frac{2d\xi_n}{c} \sqrt{\hat{\epsilon}_m}$  is the retardation factor<sup>1</sup>,  $c$  is the speed of light in vacuum and  $q$  is a dimensionless auxiliary variable.  $\hat{\epsilon}_m = \sqrt{\epsilon_m^{\parallel} \epsilon_m^{\perp}}$  and  $g_m = \epsilon_m^{\perp} / \epsilon_m^{\parallel}$  are the geometrically-averaged dielectric function and dielectric anisotropy<sup>33</sup> of  $m$ , respectively. Similar approach was also used to calculate vdW interactions of layered materials<sup>34</sup>.  $\Delta_{\text{Am}}$  and  $\Delta_{\text{Bm}}$  correspond to the dielectric mismatches following  $\Delta_{jm} = \frac{\hat{\epsilon}_j - \hat{\epsilon}_m}{\hat{\epsilon}_j + \hat{\epsilon}_m}$ , for  $j = A, B$ . Analogous to inequality (1), the vdW potential for a given EM mode  $\xi_n$  becomes positive when  $\Delta_{\text{Am}} \Delta_{\text{Bm}} < 0$ , contributing to vdW repulsion.

Using graphene (Gr), the thinnest carbon-based 2D material, as a model system, the calculated  $\hat{\epsilon}_m$  as a function of  $\hbar\xi$  for different separations are shown in Fig. 1b. The dielectric responses have the same order of magnitude with those for high-refractive-index fluids<sup>12,21,25</sup> (Supplementary Fig. S1) but the applicable

separation appears to be significantly smaller. Indeed, equation (2) suggests that the vdW repulsion can be tuned by the separation  $d$  and the dielectric anisotropy  $g_m$ , which highlight the versatility of 2D materials-mediated systems. Fig. 1b also includes the dielectric responses for the three bulk materials considered in our experiments later, including gold (Au), N,N'-bis(2-phenylethyl)perylene-3,4,9,10-bis(dicarboximide) (BPE)<sup>35,36</sup> molecular solid, and vacuum (Vac). It reveals that vdW repulsion may be observed in two sets of materials, A/m/B = Vac/Gr/Au and Au/Gr/BPE, in which the former obeys inequality (1) in all separations and frequencies and the latter for separations  $< 2$  nm.

Fig. 2a schematically presents the first system examined in this work, Vac/Gr/Au. To fabricate the structure, a sheet of chemical-vapor-deposition-grown graphene was transferred from its original substrate (copper) to a Quantifoil® holey carbon grid using a polymer-free method<sup>37</sup>, followed by annealing it in Ar/H<sub>2</sub> to remove airborne contaminants<sup>38,39</sup>. Most holes were therefore covered by freestanding monolayer graphene (Supplementary Fig. S4). Subsequently, a small amount ( $\sim 3$  ng·mm<sup>-2</sup>) of gold was evaporated in high vacuum and condensed on the sample surface at room temperature (for details see *Methods*).

The gold layer deposited on freestanding graphene is expected to not only experience a repulsive potential,  $\Phi_{\text{Rep}} = \Phi_{\text{AmB}}^{\text{vdW}}$ , but also an attractive potential,  $\Phi_{\text{Att}}$ , corresponding to the two-body vdW potential between gold and graphene,  $\Phi_{\text{mB}}^{\text{vdW}}$ <sup>30,34</sup>. The total potential acting on gold,  $\Phi_{\text{tot}} = \Phi_{\text{Att}} + \Phi_{\text{Rep}}$ , combines both effects. Our calculations show that  $\Phi_{\text{Rep}}$  is of relatively longer-range, scaling as  $d^{-1.5}$  to  $d^{-2.5}$ , for separations from  $\sim 1$  nm to  $\sim 10$  nm, as compared to  $\Phi_{\text{Att}}$  scaling as  $d^{-2.4}$  to  $d^{-2.9}$  (Fig. 2b). As a result, for  $d > 3$  nm, the vdW repulsion would overtake and result in an energy barrier height of  $\sim 20$   $\mu\text{J}\cdot\text{m}^{-2}$ , kinetically hindering the adsorption of gold on freestanding graphene. (Supplementary Section S2).

Fig. 2c shows a representative scanning electron micrograph (SEM) for gold deposited on graphene. Two regions, namely amorphous carbon (a-C) grid-supported (I) and freestanding (II) graphenes, can be identified in the inset SEM image. The morphology and density for the deposited gold clusters on regions I and II exhibit substantially different features. On region I, as expected, due to very high surface energy of gold ( $\sim 1300$  mJ·m<sup>-2</sup> at room temperature<sup>40</sup>), fast condensation at room temperature yields small spherical nanoclusters with a high nucleation density. However, on region II, despite a high degree of supercooling, the nucleation density is very low, leaving a large non-wettable area of up to  $1.3$   $\mu\text{m}^2$ , with a few large and ultrathin gold platelets grown on the surface. We performed crystallographic analysis using the Fourier-transformed scanning transmission electron microscopy (FT-STEM) on a representative hexagonal platelet (Fig. 2d). A set of Bragg diffraction spots corresponding to  $\{\frac{4}{3}\frac{2}{3}\frac{2}{3}\}$  lattice planes (lattice spacing of  $\sim 2.49$

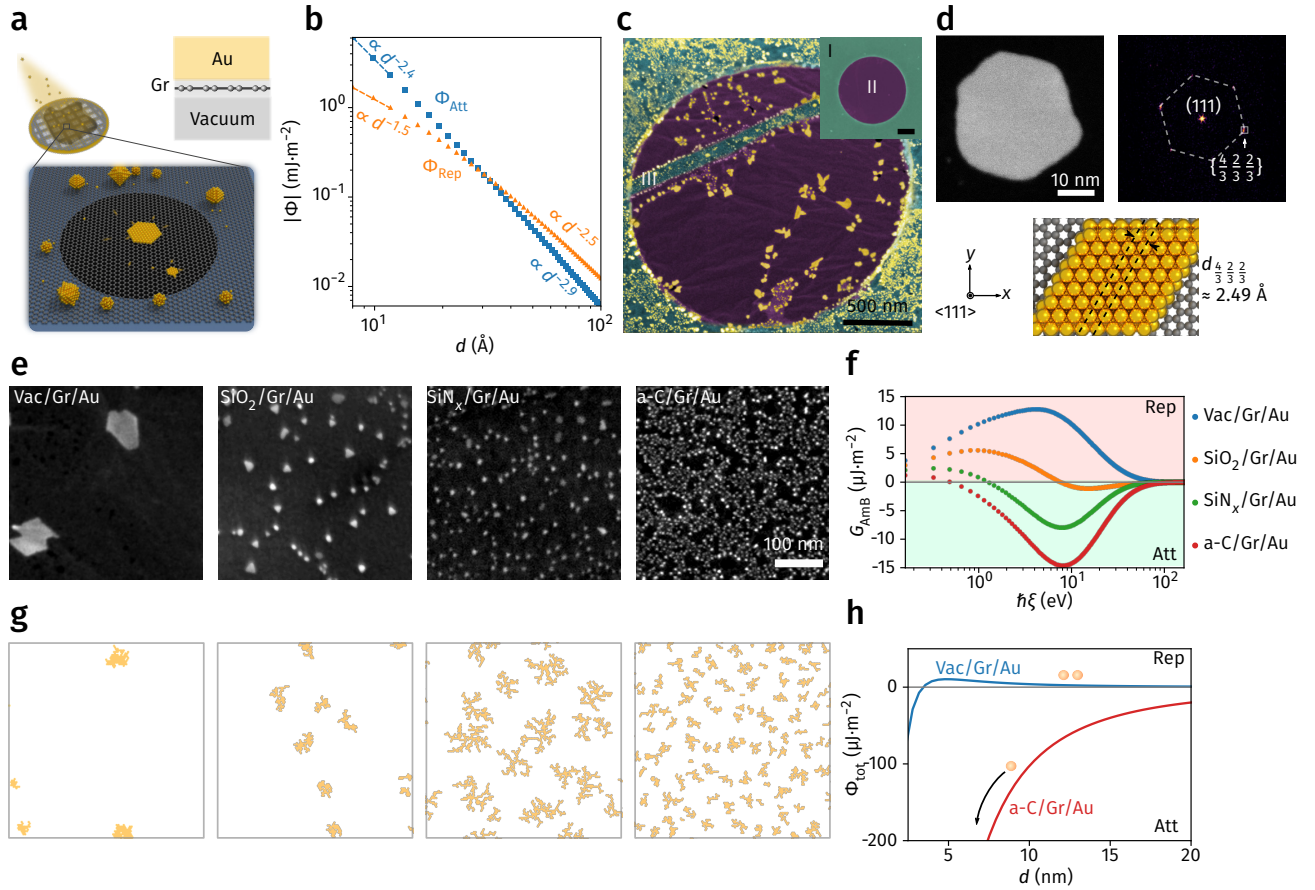


**Figure 2: Frictionless diffusion of gold atoms on freestanding graphene at room temperature.** **a.** A small amount of gold was evaporated in high vacuum and condensed at room temperature on a sheet of freestanding graphene transferred to a Quantifoil holey carbon grid. **b.** Calculated many-body repulsive potential,  $\Phi_{\text{Rep}} = \Phi_{\text{AmB}}^{\text{vdW}}$ , and two-body attractive potential,  $\Phi_{\text{Att}} = \Phi_{\text{mB}}^{\text{vdW}}$ , as a function of  $d$ . The former is of relatively long-range, scaling as  $d^{-1.5}$  to  $d^{-2.5}$ , as compared to the latter scaling as  $d^{-2.4}$  to  $d^{-2.9}$ , thereby yielding an energy barrier above graphene surface. **c.** False color SEM image for gold deposited on graphene near a hole. Inset: SEM image before gold deposition that identifies regions I and II corresponding to carbon grid-supported and freestanding graphene, respectively. Gold on freestanding graphene forms ultrathin platelets and leaves a large non-wettable area of up to  $1.3 \mu\text{m}^2$ . **d.** FT-STEM characterization of a representative hexagonal platelet (left), revealing a set of Bragg diffraction spots (right) corresponding to  $(4/3 \ 2/3 \ 2/3)$  lattice plane ( $d$ -spacing of  $\sim 2.49 \text{ \AA}$ ). **e.** SEM images for gold deposited on graphene supported by different substrates (left to right: vacuum,  $\text{SiO}_2$ ,  $\text{SiN}_x$ , and amorphous carbon (a-C)). **f.** Calculated interaction spectra  $G_{\text{AmB}}$  as a function of  $\hbar\xi$  at  $d = 0.8 \text{ nm}$  for Vac/Gr/Au,  $\text{SiO}_2/\text{Gr/Au}$ ,  $\text{SiN}_x/\text{Gr/Au}$  and a-C/Gr/Au, respectively. The full-spectrum summation is gradually converted from repulsion to attraction, yielding the increase of nucleation density in **e.** **g.** KMC simulation snapshots modeling 2D growth of gold on a surface by varying the ratio of activation energy for diffusion on pristine graphene,  $\Delta E_d^0$ , to that for binding,  $\Delta E_b$  (left to right:  $\Delta E_d^0/\Delta E_b = 0.2, 0.5, 1.0, 1.6$ ). **h.** Calculated  $\Phi_{\text{tot}}$  profiles for 6 nm thick gold platelet approaching freestanding (blue) and substrate-supported (red) graphene with respect to separation.

Å) was observed, which was only reported in the atomically-thin face-center-cubic metal crystals<sup>41</sup>. We also notice that gold deposited on the defective and contaminated domains of freestanding graphene, e.g., region III, exhibits similar behavior with that on region I.

From a thermodynamic point of view, the growth of ultrathin gold platelets on freestanding graphene would require the Au-Gr interactions to be stronger than Au surface energy, or even a negative interfacial tension<sup>2</sup>, which is unlikely and cannot explain the observed ultralow nucleation density. We further transferred graphene onto two other substrates, silicon oxide (SiO<sub>2</sub>) and silicon nitride (SiN<sub>x</sub>), and compared the morphologies of gold condensed on top (Fig. 2e). Fig. 2f presents the calculated many-body vdW interaction spectra as a function of energy,  $G_{\text{AmB}}(i\xi)$  (see equation (2)), for the four systems considered here. The full-spectrum summation indicates that in contrast to the repulsive Vac/Gr/Au system, for SiO<sub>2</sub>/Gr/Au, SiN<sub>x</sub>/Gr/Au, and a-C/Gr/Au, the vdW interactions become increasingly attractive. Together with Fig. 2e, it becomes evident that stronger vdW repulsion would lead to lower nucleation density. The growth behavior is kinetically controlled which agrees with morphological statistics of the gold nanoplatelets based on atomic force microscopy (AFM) and SEM analysis (for details see Supplementary Section S2.3).

Indeed, the classical nucleation theory suggests that the nucleation density  $N_{\text{nu}}$  is proportional to  $D^{-\frac{1}{3}}$ , where  $D$  is the surface diffusivity<sup>42</sup>. According to the SEM images in Fig. 2e, we estimate that, by making graphene freestanding, the surface diffusivity of gold was boosted by up to approximately 9 orders of magnitude (Supplementary Fig. S15), indicating the in-plane movement is nearly frictionless. The observation is further endorsed by our kinetic Monte Carlo (KMC) simulations considering the competition between Au diffusion on graphene and Au-Au binding processes on a surface (Fig. 2g and Supplementary Fig. S17). Large and sparsely distributed platelets can only be obtained when the activation energy for diffusion is negligible compared to that for Au-Au binding (see Supplementary Section S2.4).

If the vdW potential between gold and a sheet of freestanding graphene is monotonically downhill, the adsorption event of gold on the surface would be fast. Once it occurs, the thermal energy at room temperature is not sufficient to overcome the vdW well depth, thereby resulting in fast nucleation and slow diffusion, which contradicts our findings. We notice that the fabricated freestanding graphene is highly corrugated with a mean roughness greater than 2 nm (Supplementary Fig. S10 and Table S1), so the scenario of structural superlubricity observed on graphite at high temperatures<sup>43</sup> also does not apply here. The proposed physical picture, in which a vdW repulsion-induced energy barrier created above the surface hinders adsorption and offers a “highway” for in-plane movement (Fig. 2h), can nicely explain the observations.

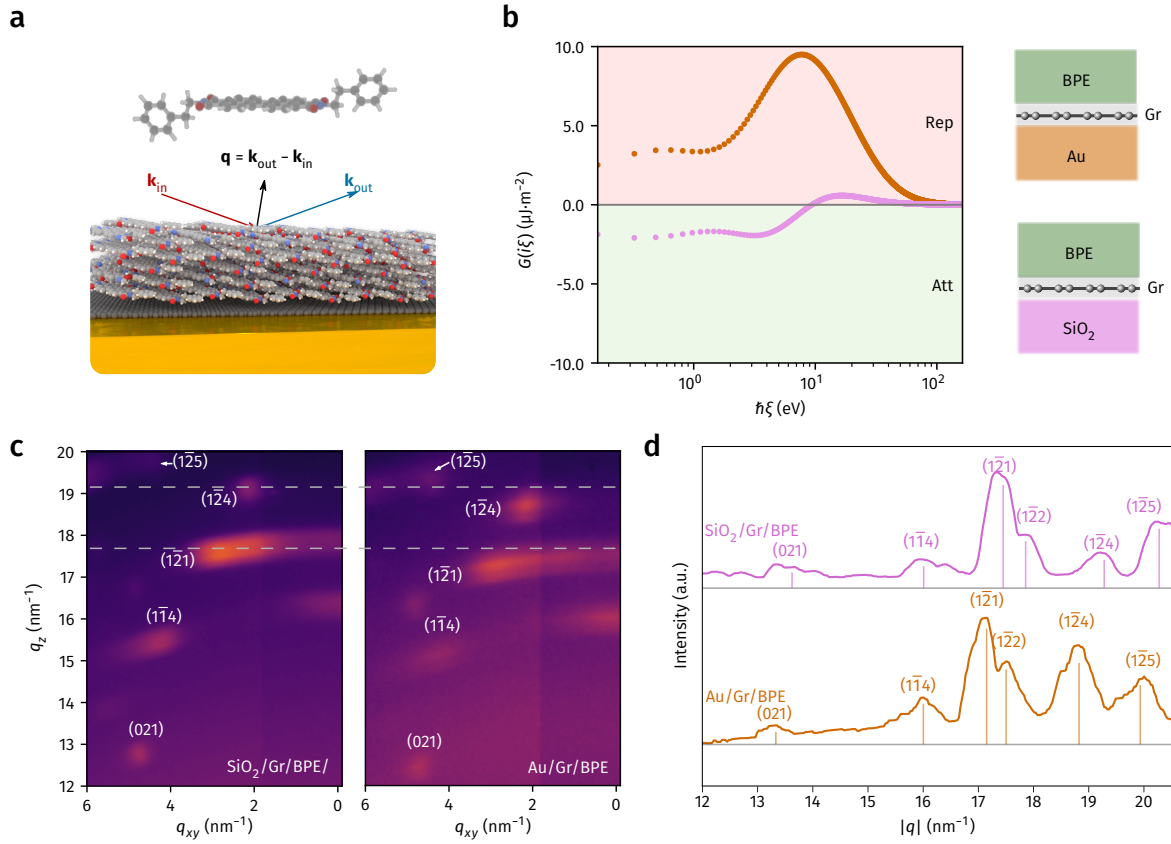


**Figure 3: vdW repulsion-induced molecular polymorphism.** **a.** Molecular structure of BPE (top) and schematic of molecular solid (bottom) having a layered crystalline structure, with the molecular plane oriented in parallel to graphene. The diffraction wave vector  $\mathbf{q}$  of a specific lattice plane follows the relation  $\mathbf{q} = \mathbf{k}_{\text{out}} - \mathbf{k}_{\text{in}}$ , where  $\mathbf{k}_{\text{in}}$  and  $\mathbf{k}_{\text{out}}$  are the wave vectors of incident and diffracted light in GIWAXS, respectively. **b.** Calculated interaction spectra  $G_{\text{AmB}}(i\xi)$  as a function of  $\hbar\xi$  for Au/Gr/BPE (orange dots) and SiO<sub>2</sub>/Gr/BPE (purple dots) systems at  $d = 1$  nm, revealing that the former yields a strong vdW repulsion and the latter has a weak attraction. **c.** Zoomed-in GIWAXS patterns for SiO<sub>2</sub>/Gr/BPE (left) and Au/Gr/BPE (right) systems showing the Laue spots corresponding to interlayer planes (12̄4) and (12̄1) near the  $q_z$  axis. As compared to SiO<sub>2</sub>/Gr/BPE, the  $q_z$  components for Au/Gr/BPE are slightly lower, confirming the interlayer d-spacings are enlarged. **d.** Comparison of integrated line cuts for SiO<sub>2</sub>/Gr/BPE, Au/Gr/BPE. The best-fitted peak positions are marked as vertical lines.

The second set of materials examined here is Au/Gr/BPE (Fig. 3a). The BPE molecule has a flat polycyclic aromatic core, perylenetetracarboxylic diimide (PTCDI), decorated with two freely rotatable phenylethyl groups on both ends. Highly ordered BPE molecular solids are of layered crystalline structure<sup>36</sup>, with the interlayer spacing determined by the sensitive balance between intermolecular  $\pi$ - $\pi$  interactions of PTCDI cores and phenylethyl groups conformational entropy<sup>44</sup>. We therefore hypothesized that, by orienting the BPE molecular plane parallel to graphene, the force exerted by the substrate across graphene may alter the interlayer spacing.

The BPE molecules were thermally evaporated onto graphene supported by gold as well as SiO<sub>2</sub> for comparison (Fig. 3b, for details see *Methods*). Fig. 3b presents the calculated  $G_{\text{AmB}}(i\xi)$  for the two systems at  $d = 0.8$  nm. Following earlier discussion in Fig. 1b, for  $d < 2$  nm, the vdW potentials between Au and BPE are always repulsive irrespective of frequency, with the main contribution from the visible to ultraviolet region. The full-spectrum summation of  $G_{\text{AmB}}(i\xi)$  according to equation (2) yields a strong vdW repulsion of  $\sim 1.3$  mJ·m<sup>-2</sup>. On the other hand, in SiO<sub>2</sub>/Gr/BPE system, the transition from attraction to repulsion at high frequencies leads to a weakly attractive potential ( $\sim -20$   $\mu$ J·m<sup>-2</sup>).

To examine the substrate interactions through graphene, we analyzed the molecular orientation and crystallographic constants of BPE molecular solids using synchrotron grazing-incidence wide-angle x-ray scattering (GIWAXS). In the GIWAXS patterns (Fig. 3c and Supplementary Fig. S23), both systems show several intense high-angle Laue spots, in particular those corresponding to the interlayer ( $1\bar{2}4$ ) and ( $1\bar{2}1$ ) planes (detailed crystallographic analysis see Supplementary Section S3) near the  $q_z$  axis, confirming the PTCDI plane is preferentially oriented parallel to the substrate<sup>45,46</sup>. However, the slightly shifted  $q_z$  components reveal polymorphs induced by the substrate force (Fig. 3c). The strongly repulsive substrate, gold, yielded interlayer spacings of 3.35 and 3.68 Å, respectively, which are enlarged by  $\sim 1.8\%$  as compared to the SiO<sub>2</sub> control. The integrated line cuts extracted from GIWAXS patterns (Fig. 3d) compares the signals for SiO<sub>2</sub>/Gr/BPE and Au/Gr/BPE. The vdW repulsion generated in Au/Gr/BPE appears to slightly offset the interlayer interactions between BPE molecules. Consequently, the effect of phenylethyl groups conformational entropy takes a more active role, increasing the interlayer spacing for a set of high- $q$  diffraction peaks ( $(1\bar{1}4)$ , ( $1\bar{2}1$ ), ( $1\bar{2}2$ ), ( $1\bar{2}4$ ) and ( $1\bar{2}5$ )) associated with the PTCDI basal plane.

We demonstrate that the vdW repulsion exists and can influence kinetics and thermodynamics of solid-state materials through 2D monolayers. In view of the growth of 2D materials family covering an increasingly large range of properties, they could become versatile surface coatings selectively repelling objects down to

atomic level, which may lead to new molecular-mechanical systems and sensors.

## Author Contributions

T.T. and C.J.S. conceived the idea and designed the experiments. T.T. and F.N. developed the theoretical framework. T.T. performed first-principle calculations under guidance of E.J.G.S. T.T., G.V. and K.C. fabricated the freestanding graphene samples and carried out Au deposition. T.T. characterized the freestanding graphene samples. F.K. performed STEM measurements. T.T. carried out KMC simulations. T.T. transferred graphene onto gold and SiO<sub>2</sub> substrates. Y.T.L. and S.W.C. deposited BPE molecules and carried out synchrotron GIWAXS under supervision of Y.C.C. T.T., Y.T.L. and Y.C.C. analyzed the GIWAXS patterns. T.T. and C.J.S. co-wrote the paper. All authors contributed to this work, read the manuscript, discussed the results, and agreed to the contents of the manuscript and supplementary materials.

## Acknowledgments

C.J.S., T.T., F.N., G.V., and K.C. are grateful for financial support from ETH startup funding and the European Research Council Starting Grant (N849229 CQWLED). T.T., G.V. and K.C. acknowledge technical support from the Scientific Center for Optical and Electron Microscopy (ScopeM) and FIRST-Center for Micro and Nanoscience of ETH Zurich. EJGS acknowledges computational resources through the UK Materials and Molecular Modeling Hub for access to THOMAS supercluster, which is partially funded by EPSRC (EP/P020194/1); CIRRUS Tier-2 HPC Service (ec131 Cirrus Project) at EPCC (<http://www.cirrus.ac.uk>) funded by the University of Edinburgh and EPSRC (EP/P020267/1); ARCHER UK National Supercomputing Service (<http://www.archer.ac.uk>) via d429 Project code. EJGS also acknowledges the EPSRC Early Career Fellowship (EP/T021578/1) and the University of Edinburgh for funding support. Y.C.C. thanks the financial support by the “Advanced Research Center for Green Materials Science and Technology” from The Featured Area Research Center Program within the framework of the Higher Education Sprout Project by the Ministry of Education (108L9006) and the Ministry of Science and Technology in Taiwan (MOST 108-3017-F-002-002 and 108-2221-E-011-047). T.T. thanks Dr. Liqing Zheng for providing gold substrates.

## References

1. Parsegian, V. A. *Van der Waals Forces: A Handbook for Biologists, Chemists, Engineers, and Physicists* Cambridge Core. (2017).
2. Israelachvili, J. N. *Intermolecular and surface forces* Third edition (Elsevier, Academic Press, Amsterdam, 2011).
3. Woods, L. M. *et al.* Materials perspective on Casimir and van der Waals interactions. *Rev. Mod. Phys.* **88**, 045003 (2016).
4. Novoselov, K. S., Mishchenko, A., Carvalho, A. & Castro Neto, A. H. 2D materials and van der Waals heterostructures. *Science* **353**, aac9439 (2016).
5. Leckband, D. & Israelachvili, J. Intermolecular forces in biology. *Q. Rev. Biophys.* **34**, 105–267 (2001).
6. Keesom, W. The second virial coefficient for rigid spherical molecules, whose mutual attraction is equivalent to that of a quadruplet placed at their centre. *Proc. R. Acad. Sci* **18**, 636–646 (1915).
7. Maitland, G. C. *Intermolecular forces: their origin and determination* (Oxford University Press, 1981).
8. London, F. The general theory of molecular forces. *Trans. Faraday Soc.* **33**, 8b–26 (1937).
9. Dzyaloshinskii, I. E., Lifshitz, E. M. & Pitaevskii, L. P. General Theory of van der Waals' Forces. *Phys.-Uspekhi* **4**, 153–176 (1961).
10. Casimir, H. B. On the attraction between two perfectly conducting plates. *K. Ned. Akad. Wet.* **51**, 793–795 (1948).
11. Casimir, H. B. G. & Polder, D. The Influence of Retardation on the London-van der Waals Forces. *Phys. Rev.* **73**, 033001 (1948).
12. Munday, J. N., Capasso, F. & Parsegian, V. A. Measured long-range repulsive Casimir–Lifshitz forces. *Nature* **457**, 170–173 (2009).
13. Milling, A., Mulvaney, P. & Larson, I. Direct Measurement of Repulsive van der Waals Interactions Using an Atomic Force Microscope. *J. Colloid Interface Sci.* **180**, 460–465 (1996).
14. Meurk, A., Luckham, P. F. & Bergström, L. Direct Measurement of Repulsive and Attractive van der Waals Forces between Inorganic Materials. *Langmuir* **13**, 3896–3899 (1997).

15. Lee, S.-w. & Sigmund, W. M. AFM study of repulsive van der Waals forces between Teflon AF<sup>TM</sup> thin film and silica or alumina. *Colloids Surf. A* **204**, 43–50 (2002).
16. Kenneth, O., Klich, I., Mann, A. & Revzen, M. Repulsive Casimir Forces. *Phys. Rev. Lett.* **89** (2002).
17. Levin, M., McCauley, A. P., Rodriguez, A. W., Reid, M. T. H. & Johnson, S. G. Casimir Repulsion between Metallic Objects in Vacuum. *Phys. Rev. Lett.* **105**, 090403 (2010).
18. Grushin, A. G. & Cortijo, A. Tunable Casimir Repulsion with Three-Dimensional Topological Insulators. *Phys. Rev. Lett.* **106**, 020403 (2011).
19. Sadhukhan, M. & Tkatchenko, A. Long-Range Repulsion Between Spatially Confined van der Waals Dimers. *Phys. Rev. Lett.* **118**, 210402 (2017).
20. Leonhardt, U. & Philbin, T. G. Quantum levitation by left-handed metamaterials. *New J. Phys.* **9**, 254–254 (2007).
21. Feiler, A. A., Bergström, L. & Rutland, M. W. Superlubricity Using Repulsive van der Waals Forces. *Langmuir* **24**, 2274–2276 (2008).
22. Zhao, R. *et al.* Stable Casimir equilibria and quantum trapping. *Science* **364**, 984–987 (2019).
23. Sabisky, E. S. & Anderson, C. H. Verification of the Lifshitz Theory of the van der Waals Potential Using Liquid-Helium Films. *Phys. Rev. A* **7**, 790–806 (1973).
24. Tabor, R. F., Manica, R., Chan, D. Y. C., Grieser, F. & Dagastine, R. R. Repulsive van der Waals Forces in Soft Matter: Why Bubbles Do Not Stick to Walls. *Phys. Rev. Lett.* **106**, 064501 (2011).
25. Boström, M., Sernelius, B. E., Brevik, I. & Ninham, B. W. Retardation turns the van der Waals attraction into a Casimir repulsion as close as 3 nm. *Phys. Rev. A* **85**, 010701 (2012).
26. Rafiee, J. *et al.* Wetting transparency of graphene. *Nat. Mater.* **11**, 217–222 (2012).
27. Shih, C.-J. *et al.* Breakdown in the Wetting Transparency of Graphene. *Phys. Rev. Lett.* **109**, 176101 (2012).
28. Li, M., Reimers, J. R., Dobson, J. F. & Gould, T. Faraday cage screening reveals intrinsic aspects of the van der Waals attraction. *Proc. Nat. Acad. Sci.* **115**, E10295–E10302 (2018).
29. Liu, X., Zhang, Z. & Guo, W. van der Waals screening by graphenelike monolayers. *Phys. Rev. B* **97**, 241411 (2018).

30. Ambrosetti, A. & Silvestrelli, P. L. Hidden by graphene – Towards effective screening of interface van der Waals interactions via monolayer coating. *Carbon* **139**, 486–491 (2018).
31. Kim, Y. *et al.* Remote epitaxy through graphene enables two-dimensional material-based layer transfer. *Nature* **544**, 340–343 (2017).
32. Kong, W. *et al.* Polarity governs atomic interaction through two-dimensional materials. *Nature Materials* **17**, 999–1004 (2018).
33. Tian, T. *et al.* Electronic Polarizability as the Fundamental Variable in the Dielectric Properties of Two-Dimensional Materials. *Nano Letters* **20**, 841–851 (2019).
34. Zhou, Y., Pellouchoud, L. A. & Reed, E. J. The potential for fast van der Waals computations for layered materials using a Lifshitz model. *2D Mater.* **4**, 025005 (2017).
35. Mizuguchi, J. N,N'-Bis(2-phenethyl)perylene-3,4:9,10-bis(dicarboximide). *Acta Cryst. C* **54**, 1479–1481 (1998).
36. Ling, M.-M. *et al.* Air-Stable n-Channel Organic Semiconductors Based on Perylene Diimide Derivatives without Strong Electron Withdrawing Groups. *Adv. Mater.* **19**, 1123–1127 (2007).
37. Regan, W. *et al.* A direct transfer of layer-area graphene. *Appl. Phys. Lett.* **96**, 113102 (2010).
38. Li, Z. *et al.* Effect of airborne contaminants on the wettability of supported graphene and graphite. *Nat. Mater.* **12**, 925–931 (2013).
39. Russo, C. J. & Passmore, L. A. Controlling protein adsorption on graphene for cryo-EM using low-energy hydrogen plasmas. *Nat. Methods* **11**, 649–652 (2014).
40. Mills, K. C. & Su, Y. C. Review of surface tension data for metallic elements and alloys: Part 1 – Pure metals. *Int. Mater. Rev.* **51**, 329–351 (2006).
41. Jin, R. *et al.* Photoinduced Conversion of Silver Nanospheres to Nanoprisms. *Science* **294**, 1901–1903 (2001).
42. Mo, Y. W., Kleiner, J., Webb, M. B. & Lagally, M. G. Activation energy for surface diffusion of Si on Si(001): A scanning-tunneling-microscopy study. *Phys. Rev. Lett.* **66**, 1998–2001 (1991).
43. Cihan, E., İpek, S., Durgun, E. & Baykara, M. Z. Structural lubricity under ambient conditions. *Nat. Commun.* **7**, 12055 (2016).

44. Schmidt, R. *et al.* High-Performance Air-Stable n-Channel Organic Thin Film Transistors Based on Halogenated Perylene Bisimide Semiconductors. *J. Am. Chem. Soc.* **131**, 6215–6228 (2009).
45. Chiu, Y.-C. *et al.* Multilevel nonvolatile transistor memories using a star-shaped poly((4-diphenylamino)benzyl methacrylate) gate electret. *NPG Asia Mater.* **5**, e35 (2013).
46. Shih, C.-J. *et al.* Partially-Screened Field Effect and Selective Carrier Injection at Organic Semiconductor/Graphene Heterointerface. *Nano Lett.* **15**, 7587–7595 (2015).

## Methods

**Calculation of vdW interaction spectra** The dielectric responses as function of imaginary frequency  $\epsilon(i\xi)$  was calculated using the Kramers Kronig relationship<sup>1</sup>:

$$\epsilon(i\xi) = 1 + \frac{2}{\pi} \int_0^{\infty} \frac{\omega \text{Im}[\epsilon(\omega)]}{\omega^2 + \xi^2} d\omega \quad (3)$$

where  $\omega$  is the real frequency, and  $\text{Im}[\epsilon(\omega)]$  is the imaginary part of complex dielectric function  $\epsilon(\omega)$ . Frequency-dependent dielectric functions of  $\text{SiO}_2$ <sup>47</sup>,  $\text{SiN}_x$ <sup>47</sup>, bromobenzene (BrPh)<sup>12</sup>, amorphous carbon<sup>48</sup>, and Au<sup>47</sup> were extracted from experimental data, respectively. The dielectric function of BPE is estimated using the single Lorentz oscillator model following  $\epsilon_{\text{BPE}}(i\xi) = 1 + \frac{\xi_p^2}{\xi_g^2 + K\xi + \xi^2}$  where  $\hbar\xi_g = 2.30$  eV,  $\hbar\xi_p = 3.16$ ,  $\hbar K = 0.1$  eV, yielding an optical refractive index  $n \approx 1.7$ . Frequency-dependent 2D polarizabilities ( $\alpha_{2D}^{\parallel}$ ,  $\alpha_{2D}^{\perp}$ ) of graphene were obtained by *ab initio* package GPAW<sup>49</sup> using the projector augmented wave method<sup>50</sup>. Dielectric responses were calculated using random phase approximation on top of the Perdew-Burke-Ernzerhof exchange-correlation functional<sup>51</sup> with plane wave cutoff energy of 500 eV, k-point density of  $15 \text{ \AA}^{-1}$  and truncated Coulomb kernel to avoid spurious interaction from periodic images.

**Graphene growth** Monolayer graphene was synthesized by chemical vapor deposition (CVD). Copper (Cu) foil (99.999%, Alfa Aesar) was first cleaned by acetone, followed by isopropanol (IPA) and electrochemically polishing in a mixture of 2:1:1:0.2 deionized water (DI- $\text{H}_2\text{O}$ ) : orthophosphoric acid : ethanol : IPA under a bias of 5 V. The polished Cu foil was then annealed in a quartz tube furnace at 1060 °C under 5 Torr and 50 standard cubic centimetres per minute (sccm) of hydrogen ( $\text{H}_2$ ) flow. The growth of graphene was followed by flowing 40 sccm of methane ( $\text{CH}_4$ ) and 15 sccm of  $\text{H}_2$  at 1000 °C under 5 Torr for 10 minutes. After cooling down, graphene on the backside of the Cu foil was etched by oxygen plasma.

**Freestanding graphene on Quantifoil grids** The Quantifoil® grids consisting of amorphous carbon film with pore opening of  $1.2 \sim 5 \mu\text{m}$  supported by Au meshes were cleaned by acetone rinsing before use. The grids were placed onto the Cu foil with the holey carbon film facing graphene. By dropping  $\sim 5 \mu\text{L}$  of IPA onto the grid and heating the Cu foil at 120 °C, the grid was adhered to graphene/Cu by capillary force during evaporation of IPA. The Cu foil was etched at the liquid-air interface of 0.5 M ammonium persulfate (APS) solution. The APS residue was rinsed with DI- $\text{H}_2\text{O}$  for several times. The grid was finally lifted from

the liquid-air interface and dried under gentle argon flow.

**Substrate-supported graphene** Monolayer graphene supported by amorphous carbon film was prepared by the same method as freestanding graphene on Quantifoil grids. Graphene films supported by SiO<sub>2</sub> and SiN<sub>x</sub> and gold were fabricated using a polymer-assisted transfer method. SiO<sub>2</sub> (300 nm thermal oxide on Si, Si-Mat) and SiN<sub>x</sub> (100 nm LPCVD low-stress nitride on Si, University Wafer) wafers were cleaned by Piranha solution (7:3 H<sub>2</sub>SO<sub>4</sub> : H<sub>2</sub>O<sub>2</sub>) before use. Ultraflat Au substrates were fabricated by the template-stripping method on silicon wafer<sup>52</sup>. Poly methylmethacrylate (PMMA, 4% solution in anisole) was spin-coated on CVD-grown graphene/Cu and baked at 120 °C. The Cu foil was etched by 0.5 M APS solution. After exchanging APS solution with DI-H<sub>2</sub>O, the PMMA/graphene film was transferred onto the desired substrate. The substrate was kept in ambient overnight and baked at 120 °C to enhance adhesion between substrate and graphene. The PMMA was removed by acetone and subsequently cleaned using IPA.

**Au deposition** Graphene samples (freestanding and substrate-supported) were all annealed under 1:1 mixture of Ar and H<sub>2</sub> at 600 °C for 2 hours to remove airborne contamination and loaded in high-vacuum evaporation chamber (Plassys MEB550S). Au was deposited by electron beam evaporation at room temperature under a pressure < 10<sup>-7</sup> mBar. The deposition rate was maintained  $\sim 5 \times 10^{-3}$  nm·s<sup>-1</sup>. The amount of gold deposited  $m_{\text{Au}}$  (mass per area) was calculated using nominal thickness  $\delta_{\text{Au}}$  as  $m_{\text{Au}} = \delta_{\text{Au}}\rho_{\text{Au}}$ , where  $\rho_{\text{Au}} = 19.30$  g·cm<sup>-3</sup> is the density of gold.

**BPE deposition** Thin film epitaxy of BPE onto the desired substrates were carried out in a home-made physical vapor deposition (PVD) chamber at pressure below 10<sup>-5</sup> mBar while the substrates are heated up to 80 °C to facilitate formation of crystalline structures. The deposition rate was kept at 0.1 nm·s<sup>-1</sup> and final thickness of BPE was  $\sim 50$  nm.

**GIWAXS characterizations** GIWAXS analysis was conducted on beamline BL13A at the National Synchrotron Radiation Research Center of Taiwan. The incidence angle and beam energy of the X-ray were 0.12 and 12.16 keV, corresponding to a wavelength of 1.02143 Å. All of GIWAXS images were collected in reflection mode by MAR165 CCD with a 2D area detector.

**Electron microscopy** SEM characterizations were carried out on Zeiss ULTRA plus with 3 kV beam voltage and 20  $\mu\text{m}$  aperture. Scanning transmission electron microscopy (STEM) images were acquired with a high-angle annular dark field (HAADF) detector both at cryogenic conditions using a liquid-nitrogen-cooled holder (Gatan) on a Hitachi HD 2700 CS (operation voltage 200 kV). Fourier transformation was performed on the phase contrast images.

**AFM characterizations** AFM topographies of graphene samples were performed on Bruker Resolve using the PeakForce Tapping mode combined with ScanAsyst Air ultrasharp probe to overcome noise artifacts on freestanding films caused by standard tapping mode scanning<sup>53</sup>. Force setpoint were maintained under 500 pN to avoid breaking of graphene sheet.

**KMC simulations** 2D diffusion of Au atoms on graphene surface was simulated by standard n-fold KMC algorithm on a triangular lattice with at least 200 mesh grids in both  $x$ - and  $y$ -directions. The following three events were considered: (i) deposition of atoms, (ii) diffusion on pristine graphene, (iii) diffusion on defective area and (iv) interatomic binding, corresponding to kinetic energy barriers of  $\Delta E_e$ ,  $\Delta E_d^0$ ,  $\Delta E_d^*$  and  $\Delta E_b$ , respectively. Rate  $r_i$  of individual event  $i$  was calculated using  $r_i = \nu_0 \exp(-\frac{\Delta E_i}{k_B T})$ , where  $\nu_0$  is the rate prefactor, and the probability of event  $i$ ,  $p_i$ , follows:  $p_i = r_i n_i / \sum_i r_i n_i$ , where  $n_i$  is the degeneracy of event  $i$ . More details for the parameters used in the simulations see Supplementary Information.

## References for Methods

47. *Handbook of optical constants of solids* (ed Palik, E. D.) (Academic Press, 1998).
48. Gioti, M. & Logothetidis, S. Dielectric function, electronic properties and optical constants of amorphous carbon and carbon nitride films. *Diam. Relat. Mater.* **12**, 957–962 (2003).
49. Mortensen, J. J., Hansen, L. B. & Jacobsen, K. W. Real-space grid implementation of the projector augmented wave method. *Phys. Rev. B* **71**, 035109 (2005).
50. Kresse, G. & Joubert, D. From ultrasoft pseudopotentials to the projector augmented-wave method. *Phys. Rev. B* **59**, 1758–1775 (1999).
51. Perdew, J. P., Burke, K. & Ernzerhof, M. Generalized Gradient Approximation Made Simple. *Phys. Rev. Lett.* **77**, 3865–3868 (1996).

52. Hegner, M., Wagner, P. & Semenza, G. Ultralarge atomically flat template-stripped Au surfaces for scanning probe microscopy. *Surf. Sci.* **291**, 39–46 (1993).
53. Clark, N., Oikonomou, A. & Vijayaraghavan, A. Ultrafast quantitative nanomechanical mapping of suspended graphene. *Phys. Status Solidi B* **250**, 2672–2677 (2013).

# Supporting Information for: **Solid-State Lifshitz-van der Waals Repulsion through Two-Dimensional Materials**

Tian Tian<sup>1</sup>, Franzisca Naef<sup>1</sup>, Gianluca Vagli<sup>1</sup>, Kemal Celebi<sup>1</sup>, Yen-Ting Li<sup>2,3</sup>,  
Shu-Wei Chang<sup>2</sup>, Frank Krumeich<sup>4</sup>, Elton J. G. Santos<sup>5</sup>, Yu-Cheng Chiu<sup>2</sup>, and  
Chih-Jen Shih <sup>\*1</sup>

<sup>1</sup>Institute for Chemical and Bioengineering, ETH Zürich, CH-8093 Zürich,  
Switzerland

<sup>2</sup>Department of Chemical Engineering, National Taiwan University of Science  
and Technology, Taipei 10607, Taiwan

<sup>3</sup>National Synchrotron Radiation Research Center, Hsinchu 30076, Taiwan

<sup>4</sup>Laboratory of Inorganic Chemistry, ETH Zürich, 8093, Zürich, Switzerland

<sup>5</sup>Institute for Condensed Matter Physics and Complex Systems, School of Physics  
and Astronomy, The University of Edinburgh, EH9 3FD, UK.

---

\*Correspondence to C.-J.S. [chih-jen.shih@chem.ethz.ch](mailto:chih-jen.shih@chem.ethz.ch)

# S1 Theoretical Simulations

## S1.1 Modified Lifshitz theory for anisotropic media

The derivation of equation 2 is described as follows.. The vdW interaction energy of  $\Phi_{\text{AmB}}^{\text{vdW}}$  corresponding to the total energy summed from all allowed EM modes<sup>S1</sup>, is given by:

$$\Phi_{\text{AmB}}^{\text{vdW}} = \frac{k_B T}{2(2\pi)^2} \sum_{n=-\infty}^{\infty} \int_{r_n}^{\infty} \ln D(i\xi_n, \mathbf{k}) d^2\mathbf{k} \quad (\text{S1})$$

where  $\mathbf{k} = (k_x, k_y)$  is the in-plane wavevector, and  $D(i\xi_n, \mathbf{k})$  is the dispersion relation for a given geometry.

For generality, the dielectric tensor of material j has diagonal components  $\epsilon_j^{xx}$ ,  $\epsilon_j^{yy}$  and  $\epsilon_j^{zz}$ . By transforming

$\mathbf{k} = (\kappa \cos \vartheta, \kappa \sin \vartheta)$ , and  $g_j = \left[ \frac{\epsilon_j^{xx}}{\epsilon_j^{zz}} \cos^2 \vartheta + \frac{\epsilon_j^{yy}}{\epsilon_j^{zz}} \sin^2 \vartheta \right]^{-1}$  where  $\kappa, \vartheta$  are the corresponding polar coordinates of  $\mathbf{k}$ , the dispersion relation  $D$  of an anisotropic A/m/B layered system follows<sup>S2</sup>:

$$D = 1 - \underbrace{\left[ \frac{\hat{\epsilon}_A - \epsilon_m^{zz} g_m^{1/2}(\vartheta)}{\hat{\epsilon}_A + \epsilon_m^{zz} g_m^{1/2}(\vartheta)} \right]}_{\Delta_{\text{Am}}} \underbrace{\left[ \frac{\hat{\epsilon}_B - \epsilon_m^{zz} g_m^{1/2}(\vartheta)}{\hat{\epsilon}_B + \epsilon_m^{zz} g_m^{1/2}(\vartheta)} \right]}_{\Delta_{\text{Bm}}} e^{-2g_m^{1/2}(\vartheta)\kappa d} \quad (\text{S2})$$

$$= 1 - \Delta_{\text{Am}}(\vartheta)\Delta_{\text{Bm}}(\vartheta)e^{-2g_m^{1/2}(\vartheta)\kappa d}$$

By further introducing an auxiliary variable  $x = 2g_m^{1/2}(\vartheta)\kappa d$ , it follows:

$$\Phi_{\text{AmB}}^{\text{vdW}} = \frac{k_B T}{32\pi^2 d^2} \sum_{n=-\infty}^{\infty} \int_0^{2\pi} g_m(i\xi_n, \vartheta) d\vartheta \int_{r_n}^{\infty} x dx \ln[1 - \Delta_{\text{Am}}(i\xi_n, \vartheta)\Delta_{\text{Bm}}(i\xi_n, \vartheta)e^{-x}] \quad (\text{S3})$$

Accordingly, equation (2) is obtained for  $\epsilon_m^{xx} = \epsilon_m^{yy}$ , i.e.  $g_m$  is independent of  $\vartheta$ , which is valid for most 2D materials where the 2D lattice is hexagonal or square. Moreover, in equation (2),  $\hat{\epsilon}_A$  and  $\hat{\epsilon}_B$  reduce to  $\epsilon_A$  and  $\epsilon_B$ , respectively, when A and B are isotropic bulk materials. Time-reversal symmetry  $\epsilon(i\xi) = \epsilon(-i\xi)$  is used when magnetic response of the material is negligible, therefore equation (2) only needs to be evaluated for  $\xi_n \geq 0$ . Moreover, our numerical analysis suggests the integral of  $\Phi_{\text{AmB}}^{\text{vdW}}$  is dominated by  $x \leq 5$ , or equivalently  $\kappa \leq 2.5(g_m d)^{-1}$ . When  $d$  is in the order of 2 nm, and  $g_m = 2.5$ , the majority of interaction comes from EM modes with  $\kappa < 0.05 \text{ \AA}^{-1}$ . In other words, evaluating equation (2) using the material dielectric functions at the optical limit ( $\mathbf{k} \rightarrow 0$ ) would preserve the accuracy of calculated  $\Phi_{\text{AmB}}$ .

Complementary to Fig. 1b, Fig. S1 compares the dielectric responses of other materials studied here.

Notably, at the order of  $d = 1$  nm,  $\hat{\epsilon}_m$  of graphene is comparable to that of bromobenzene (BrPh), a high-refractive-index liquid commonly used in experiments demonstrating Casimir repulsion<sup>S3,S4</sup>. In this respect, 2D material appears to be a promising candidate for realizing repulsive vdW interactions. However, unlike bulk liquid,  $\hat{\epsilon}_m$  of a 2D material strongly depends on the separation  $d$ , making the repulsion more pronounced at short distances (the vdW regime).

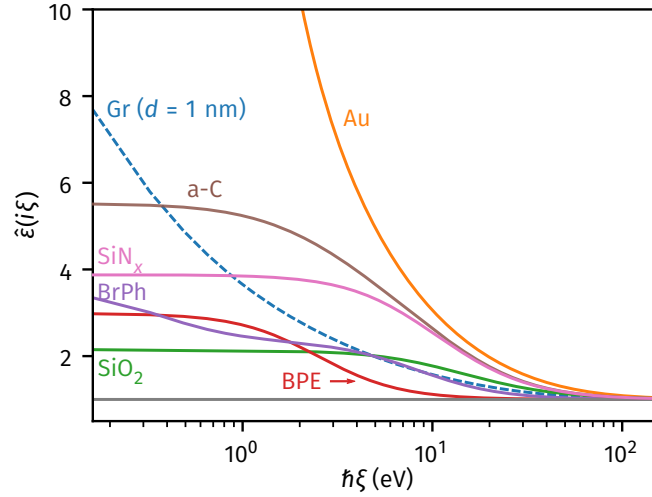


Figure S1: **Comparison of  $\hat{\epsilon}(i\xi)$  responses for materials considered in this study.** The effective dielectric function of graphene at  $d = 1$  nm is higher than that of the widely-used high-refractive-index liquid bromobenzene (BrPh).

## S1.2 Attractive and repulsive interactions in the Vac/Gr/Au system

The Lifshitz formalism in equation 2 corresponds to the AmB systems when A and B are semi-infinite. In order to model the interactions of atomically-thin Au platelets, a multilayer approach was used to calculate  $\Phi_{\text{AmB}}^{\text{vdW}}$  as shown in Fig. S2 inset. The thickness of the Au layer is  $\delta_{\text{Au}}$ , and the effective thickness of graphene is  $\delta_{\text{Gr}}$ .

The repulsive interaction  $\Phi_{\text{Rep}}$  at separation  $d$  is similar to equation 2, with different expression of the

dispersion relation<sup>S2</sup>:

$$\Phi_{\text{Rep}}(d, \delta_{\text{Au}}) = \frac{k_{\text{B}}T}{16\pi d^2} \sum_{n=-\infty}^{\infty} \int_{r_n}^{\infty} x \ln [1 - \Delta_{\text{L}}^*(i\xi_n)\Delta_{\text{R}}^*(i\xi_n)e^{-x}] dx \quad (\text{S4})$$

$$\Delta_{\text{L}}^* = \Delta_{\text{Vac/m}}$$

$$\Delta_{\text{R}}^* = \frac{\Delta_{\text{Vac/Au}}e^{-x\frac{\delta_{\text{Au}}}{d}} + \Delta_{\text{Au/m}}}{1 + \Delta_{\text{Vac/Au}}\Delta_{\text{Au/m}}e^{-x\frac{\delta_{\text{Au}}}{d}}}$$

where the expressions for  $\Delta_{\text{Vac/m}}$  and  $\Delta_{\text{Au/m}}$  are analogous to those of  $\Delta_{\text{Am}}$  and  $\Delta_{\text{Bm}}$  in a A/m/B system, respectively.

In the platelet system, there is also two-body attractive interaction between graphene and the Au platelet. The attractive potential between freestanding graphene and Au platelet  $\Phi_{\text{Att}}$  results from the vacuum spacing between the surfaces of graphene and Au<sup>S5,S6</sup>. Different from the repulsive potential, the attractive potential has a shorter distance  $d^* = d - \delta_{\text{Gr}}$ . The graphene layer is treated as a dielectric material with the effective dielectric tensor  $\epsilon_{\text{Gr}}$  same as bulk graphite and thickness  $\delta_{\text{Gr}}$ . Note despite the breakdown of continuum dielectric function for atomically thin materials, such effective treatment in Lifshitz theory can still produce quantitatively correct energy values as compared to other computationally expensive approaches, such as *ab initio* quantum chemistry simulations.<sup>S5</sup>. Similar to equation (S4),  $\Phi_{\text{Att}}$  of the multilayer configuration is given by:

$$\Phi_{\text{Att}}(d, \delta_{\text{Au}}) = \frac{k_{\text{B}}T}{16\pi(d^*)^2} \sum_{n=-\infty}^{\infty} \int_{r_n}^{\infty} x \ln [1 - \Delta_{\text{L}}^*(i\xi_n)\Delta_{\text{R}}^*(i\xi_n)e^{-x}] dx \quad (\text{S5})$$

$$\Delta_{\text{L}}^* = \frac{\Delta_{\text{Vac/Gr}}e^{-x\frac{\delta_{\text{Gr}}}{d^*}} + \Delta_{\text{Gr/Vac}}}{1 + \Delta_{\text{Vac/Gr}}\Delta_{\text{Gr/Vac}}e^{-x\frac{\delta_{\text{Gr}}}{d^*}}}$$

$$\Delta_{\text{R}}^* = \frac{\Delta_{\text{Vac/Au}}e^{-x\frac{\delta_{\text{Au}}}{d^*}} + \Delta_{\text{Au/Vac}}}{1 + \Delta_{\text{Vac/Au}}\Delta_{\text{Au/Vac}}e^{-x\frac{\delta_{\text{Au}}}{d^*}}}$$

Equation (S5) can be further generalized to calculate the two-body attraction in the bulk Vac/Gr/Au

system, corresponding to  $\delta_{\text{Au}} \rightarrow \infty$ :

$$\begin{aligned}\Phi_{\text{Att}}^{\text{Bulk}}(d) &= \frac{k_{\text{B}}T}{16\pi(d^*)^2} \sum_{n=-\infty}^{\infty} \int_{r_n}^{\infty} x \ln [1 - \Delta_{\text{L}}^*(i\xi_n)\Delta_{\text{R}}^*(i\xi_n)e^{-x}] dx \\ \Delta_{\text{L}}^* &= \frac{\Delta_{\text{Vac/Gr}}e^{-x\frac{\delta_{\text{Gr}}}{d^*}} + \Delta_{\text{Gr/Vac}}}{1 + \Delta_{\text{Vac/Gr}}\Delta_{\text{Gr/Vac}}e^{-x\frac{\delta_{\text{Gr}}}{d^*}}} \\ \Delta_{\text{R}}^* &= \Delta_{\text{Au/Vac}}\end{aligned}\tag{S6}$$

Equation S6 was used to calculate  $\Phi_{\text{Att}}$  in Fig. 2b. For a bulk Vac/Gr/Au system, when the separation is much larger than  $\delta_{\text{Gr}}$ , we have  $d \approx d^*$ . We notice that when  $d \rightarrow \infty$ ,  $\Phi_{\text{Att}}$  reduces to the interaction form between a 2D sheet and semi-infinite bulk material, scaling as  $\Phi_{\text{Att}} \propto d^{-3}$ , while  $\Phi_{\text{Rep}}$  reduces to the interaction between two semi-infinite bulk materials in vacuum, yielding  $\Phi_{\text{Rep}} \propto d^{-2}$ .

The difference in scaling laws between  $\Phi_{\text{Att}}$  and  $\Phi_{\text{Rep}}$  results in a repulsive energy barrier beyond  $d > 3$  nm, as shown in Fig. S2. As expect, we observe that the barrier decreases with thinner Au layer. The calculated magnitude of the barrier ( $\sim 20 \mu\text{J}\cdot\text{m}^{-2}$  in the bulk Vac/Gr/Au system) is significantly smaller than the surface energy of graphene or gold and can be overcome by thermal energy at room temperature. For example, consider a sub-monolayer of Au atoms on 2D surface with the surface coverage  $\lambda$ , the thermal kinetic energy can be estimated using  $E_{\text{kin}} = \lambda k_{\text{B}}T N_{\text{c}}/S_{\text{c}}$  where  $N_{\text{c}}$  and  $S_{\text{c}}$  are the number of atoms and the area of the 2D unit cell, respectively. The thermal activation energy can be overcome when  $\lambda > 4 \times 10^{-4}$ , which is much lower than the experimental condition. Therefore, we still expect to see nucleation on the free-standing graphene surface, while the nucleation density is greatly suppressed due to the existence of such repulsive barrier.

### S1.3 Attractive interactions in substrate-supported systems

The analysis in section S1.2 can be easily extended to model the interactions between substrate (Sub) - supported graphene and a thin layer of gold. Assume the substrate has isotropic dielectric response  $\epsilon_{\text{Sub}}$ , the attractive interaction between a substrate-supported graphene and Au layer,  $\Phi_{\text{Att}}^{\text{ss}}$  (to be distinguished from

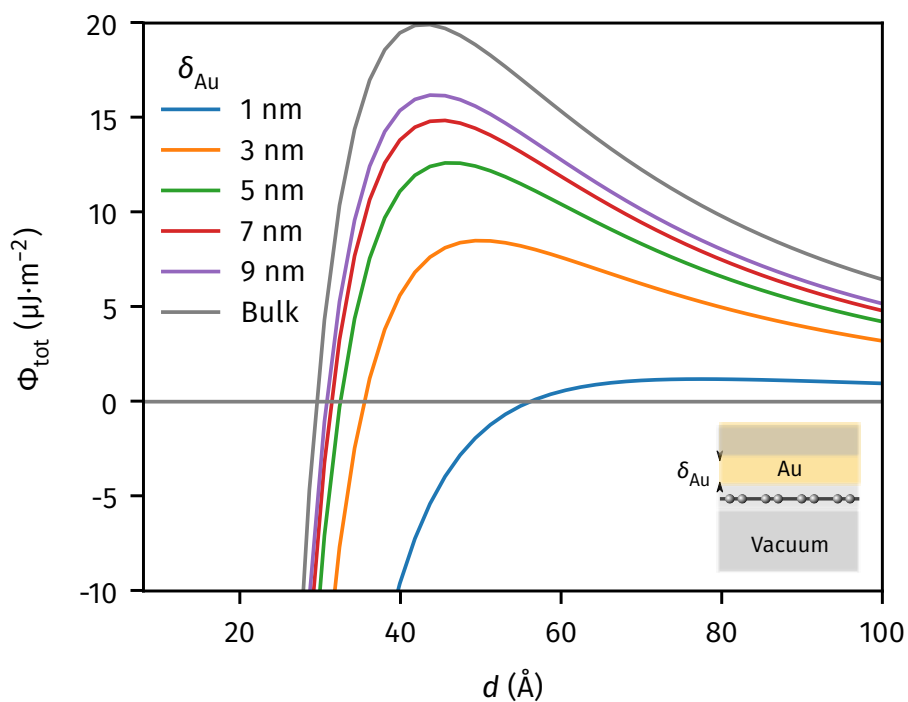


Figure S2: **Total vdW potential  $\Phi_{\text{tot}}$  as a function of Au-Gr distance  $d$  for different Au layer thickness  $\delta_{\text{Au}}$  calculated from multi-layer Lifshitz approach.** A tiny repulsive potential barrier exists when  $\delta_{\text{Au}} > 1$  nm, and saturates at  $\sim 20 \mu\text{J}\cdot\text{m}^{-2}$  for the bulk Au layer, as a result of different power laws between attractive and repulsive interactions shown in Fig. 2b.

that of a freestanding Gr/Au system) is given by:

$$\begin{aligned}\Phi_{\text{Att}}^{\text{ss}}(d, \delta_{\text{Au}}) &= \frac{k_{\text{B}}T}{16\pi(d^*)^2} \sum_{n=-\infty}^{\infty} \int_{r_n}^{\infty} x \ln [1 - \Delta_{\text{L}}^*(i\xi_n)\Delta_{\text{R}}^*(i\xi_n)e^{-x}] dx \\ \Delta_{\text{L}}^* &= \frac{\Delta_{\text{Sub/Gr}} e^{-x\frac{\delta_{\text{Gr}}}{d^*}} + \Delta_{\text{Gr/Vac}}}{1 + \Delta_{\text{Sub/Gr}}\Delta_{\text{Gr/Vac}} e^{-x\frac{\delta_{\text{Gr}}}{d^*}}} \\ \Delta_{\text{R}}^* &= \frac{\Delta_{\text{Vac/Au}} e^{-x\frac{\delta_{\text{Au}}}{d^*}} + \Delta_{\text{Au/Vac}}}{1 + \Delta_{\text{Vac/Au}}\Delta_{\text{Au/Vac}} e^{-x\frac{\delta_{\text{Au}}}{d^*}}}\end{aligned}\quad (\text{S7})$$

and subsequently the (two-body) attractive interaction between substrate-supported graphene and bulk gold is given by:

$$\begin{aligned}\Phi_{\text{Att}}^{\text{ss,Bulk}}(d) &= \frac{k_{\text{B}}T}{16\pi(d^*)^2} \sum_{n=-\infty}^{\infty} \int_{r_n}^{\infty} x \ln [1 - \Delta_{\text{L}}^*(i\xi_n)\Delta_{\text{R}}^*(i\xi_n)e^{-x}] dx \\ \Delta_{\text{L}}^* &= \frac{\Delta_{\text{Sub/Gr}} e^{-x\frac{\delta_{\text{Gr}}}{d^*}} + \Delta_{\text{Gr/Vac}}}{1 + \Delta_{\text{Sub/Gr}}\Delta_{\text{Gr/Vac}} e^{-x\frac{\delta_{\text{Gr}}}{d^*}}} \\ \Delta_{\text{R}}^* &= \Delta_{\text{Au/Vac}}\end{aligned}\quad (\text{S8})$$

where the term  $\Delta_{\text{Sub/Gr}}$  corresponds to the dielectric mismatch between the substrate and graphene interface. Such method is used to construct the potential-distance curve in Fig. 2h. As seen from equation (S8),  $\Delta_{\text{Sub/Gr}}$  has considerable influence on the attractive potential, due to the atomic thickness of graphene (i.e.  $\delta_{\text{Gr}} \ll d^*$ ). In other words,  $\Phi_{\text{Att}}$  between Sub/Gr and gold platelet also depends on  $\epsilon_{\text{Sub}}$ . Such effect is clearly different from the classical vdW description of 2D material interfaces, where the attractive two-body potential is independent of the type of substrate<sup>S7,S8</sup>. As an example, the  $\Phi_{\text{tot}}$  and  $\Phi_{\text{Att}}$  as functions of  $d$  for Vac/Gr/Au and a-C/Gr/Au systems when  $\delta_{\text{Au}} = 6$  nm (corresponding to Fig. 2h) are shown in Fig. S3. We observe the  $\Phi_{\text{tot}}$  for a-C/Gr/Au system to be significantly stronger (more negative) than that for Vac/Gr/Au over the whole  $d$ -range. Therefore, it is clear that only in Vac/Gr/Au system can an overall repulsive vdW barrier be observed.

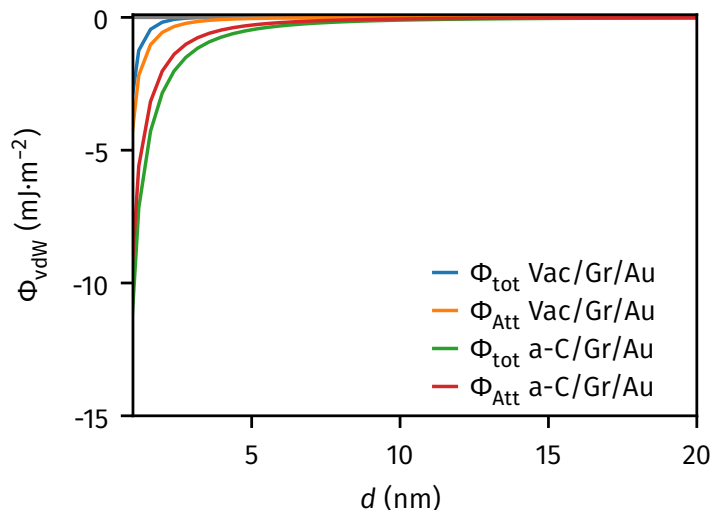


Figure S3:  $\Phi_{\text{tot}}$  and  $\Phi_{\text{Att}}$  profiles as functions of  $d$  for Vac/Gr/Au and a-C/Gr/Au systems when  $\delta_{\text{Au}} = 6$  nm. The  $\Phi_{\text{tot}} - d$  profiles are the same as those in Fig. 2h while with much larger  $y$ -axis range. In both cases, the attractive interaction dominates at short distance.

## S2 Au epitaxy on graphene surfaces

### S2.1 Relation between graphene quality and Au morphology

We have used multiple characterization techniques to examine the quality of gold deposited on freestanding graphene. As shown in Fig S4a and S4b, after the wet transfer process, >75% pores of the Quantifoil grid are covered by monolayer graphene. Raman spectroscopy (Renishaw inVia™ confocal Raman, laser 532 nm) of a typical pore (Fig. S4c) showed that the intensity ratio between the 2D and G resonance peaks ( $I_{2D}/I_G$ ) is uniformly higher than 1.5 inside the pore region, indicating the successful transfer of monolayer graphene. Annealing of the wet-transferred samples under Ar/H<sub>2</sub> environment had minimal influence on the quality of the monolayer graphene with no significant increase of D peak intensity, as shown in Fig. S4d.

The method in this study can be used to fabricate Au nanostructures on freestanding graphene samples with varied pore size and supporting substrate. As shown in Fig. S5a and S5b, similar nanostructure morphology was observed for Vac/Gr/Au with 1.2  $\mu\text{m}$  and 2.0  $\mu\text{m}$  pores on amorphous carbon grids, respectively. In addition, we also fabricated freestanding graphene samples suspended on perforated SiN<sub>x</sub> chips. The SiN<sub>x</sub> chips with pore opening ranging from 1.5 ~ 20  $\mu\text{m}$  were fabricated according to Ref. [S9]. CVD-grown graphene coated with Poly(methyl methacrylate) (PMMA) was transferred onto the holes using standard wet-etching process<sup>S10</sup>. After completely drying in ambient, the PMMA/Gr/SiN<sub>x</sub> stack was directly annealed

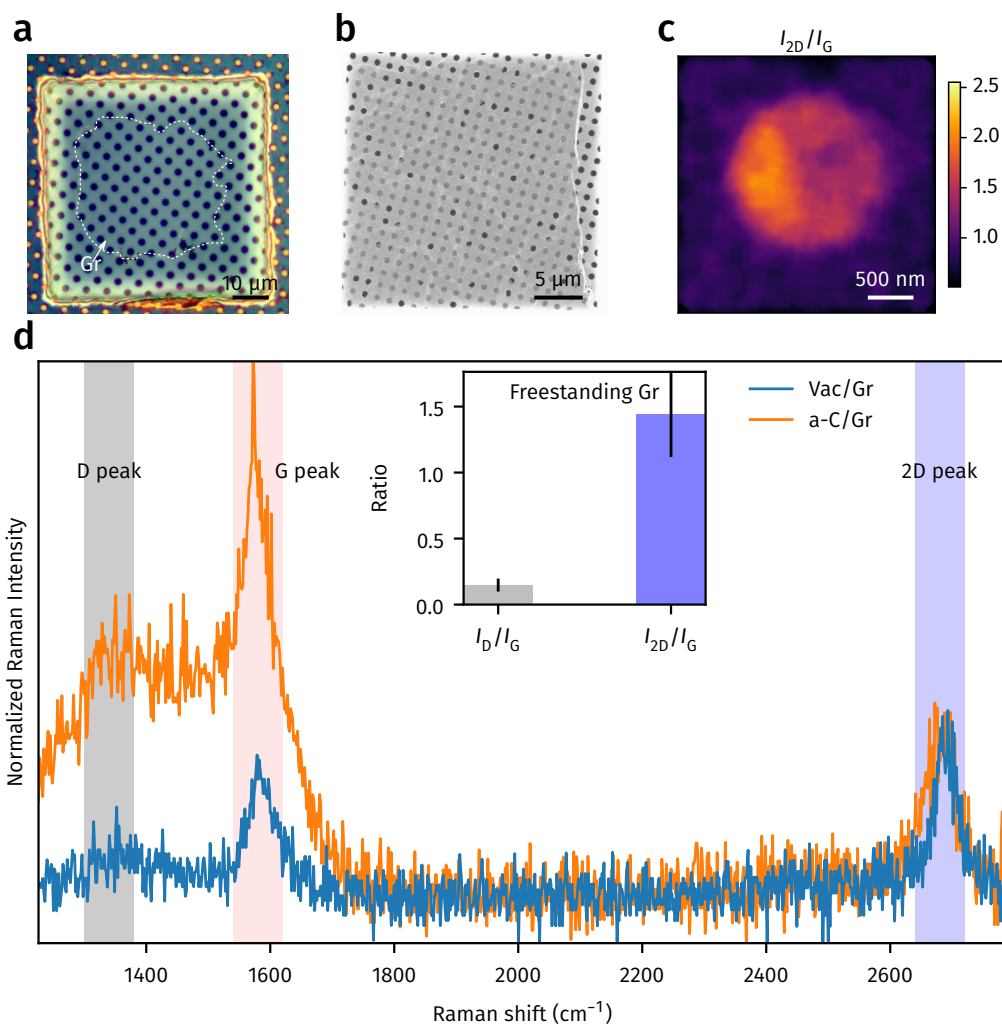


Figure S4: **Characterization of freestanding graphene fabricated by the polymer-free transfer method.** **a** Optical micrograph of free-standing graphene covered on Quantifoil holes. The boundary of graphene is identified by white dashed line. **b** SEM image of graphene-covered Quantifoil grid showing high yield. **c** 2D Raman mapping of the intensity ratio between 2D and G peaks near a graphene-covered hole. **d** Typical single-spot Raman spectra for freestanding graphene (blue) and graphene sitting on a-C (orange) after annealing, showing minimal influence of annealing on the defect density. The averaged  $I_D/I_G$  and  $I_{2D}/I_G$  ratio values of >50 samples are shown in the inset.

under Ar/H<sub>2</sub> environment at 600 °C to remove polymer coating. Although the radicals generated during the thermal decomposition of PMMA might bond with defective graphene surface<sup>S11</sup>, as shown in Fig. S5c, at sub- $\mu\text{m}$  scale, the Au nucleation density on freestanding graphene transferred on perforated SiN<sub>x</sub> substrates is similar to the samples prepared without polymer, indicating the successful fabrication of clean graphene surfaces using both methods.

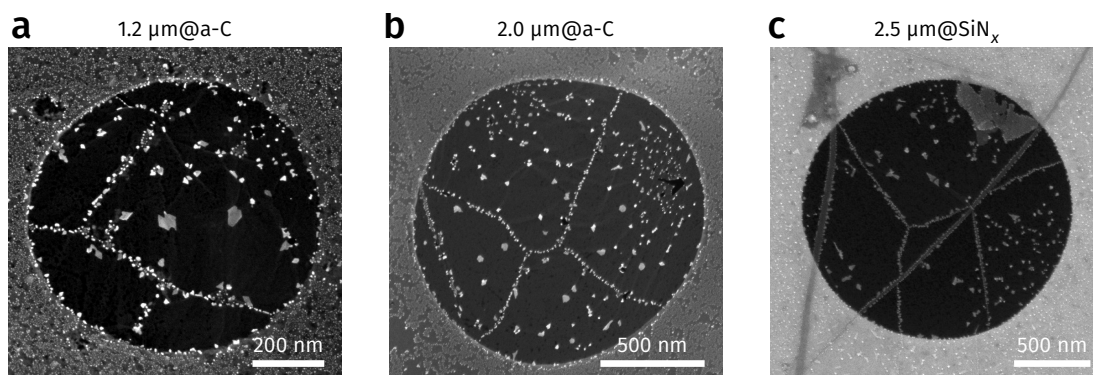


Figure S5: **SEM images of Au deposited on graphene-covered holes on various pore sizes and substrates: a** 1.2  $\mu\text{m}$  pore on a-C support, **b** 2.0  $\mu\text{m}$  pore on a-C support, and **c** 2.5  $\mu\text{m}$  pore on SiN<sub>x</sub> support.

We also investigated the Au morphology change on freestanding and supported graphene by varying the amount of evaporation. As shown in Fig. S6, when Au evaporation increased from 2.9 ng·mm<sup>-2</sup> to 19.5 ng·mm<sup>-2</sup> (corresponding to nominal thickness of 0.15 nm to 1 nm, respectively), the nucleation density on the freestanding graphene remained lower than that on a-C/Gr. When > 9.7 ng·mm<sup>-2</sup> of Au was evaporated, coalescence of Au platelets was observed which formed larger nanostructures. It is worth noting that these interconnected platelets substantially differs the dendritic Au patterns grown on graphite surface at room temperature<sup>S12,S13</sup>, which we will further explain using KMC simulations in section S2.4, as an indirect evidence of ultra-fast in-plane movement of Au on freestanding graphene.

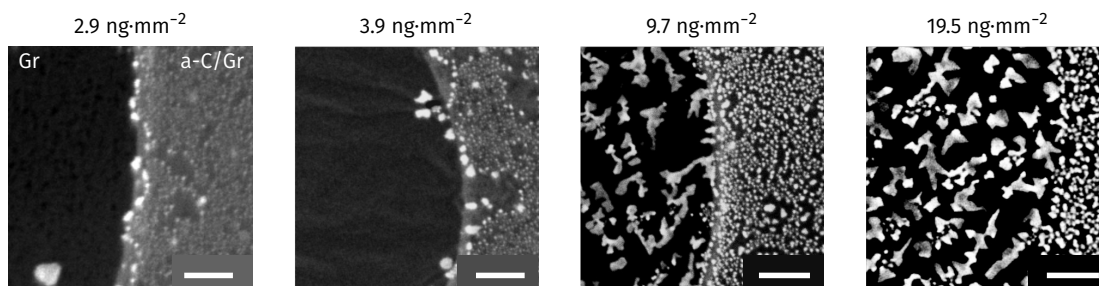


Figure S6: **Morphology of Au nanostructures by varying amount of evaporation.** Scale bars: 100 nm.

Despite a low defect density in the CVD-grown graphene as indicated by Raman spectroscopy, atomistic defects and contamination still have strong influence on the Au deposition process. Electron micrographs in

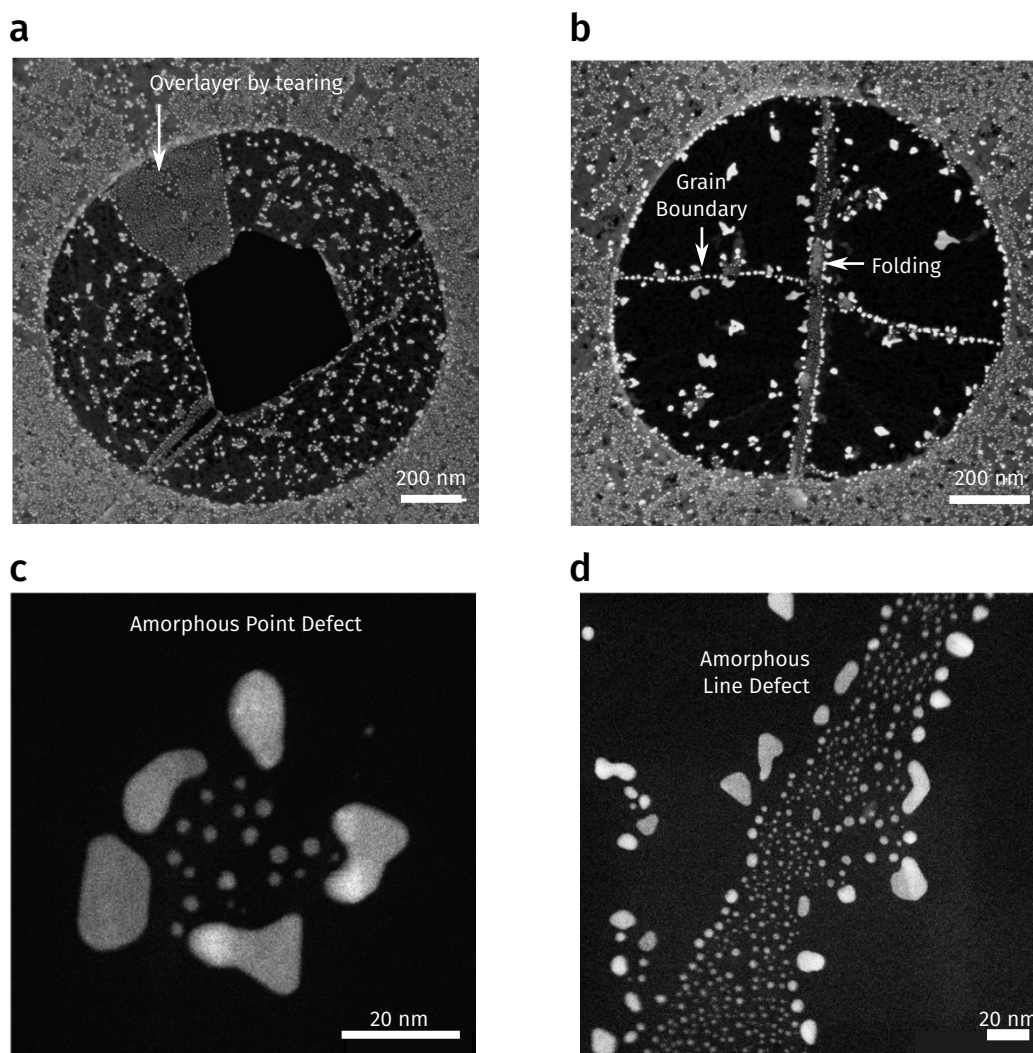


Figure S7: **Different types of high-nucleation-density areas on freestanding graphene due to surface defects and contamination.** **a** SEM image of high-nucleation-density Au deposited on overlayer graphene formed due to tearing. **b** SEM image of high-nucleation-density Au grown near the line defect and folded regions on freestanding graphene. **c** STEM image showing the morphology of Au deposited near a point contamination site on freestanding graphene. **d** STEM image of the Au morphology near a line defect. In both cases, smaller spherical particles are formed on the contaminated area, surrounded by larger planar structures, as a result of different diffusivities on different surfaces.

Fig. S7 demonstrate different types of high-nucleation-density Au nanostructures on defective or contaminated areas of freestanding Gr. As shown in Fig. S7a and S7b, high density Au particles were observed on

mechanical defects of graphene surface, such as (i) overlayer (ii) folding and (iii) grain boundary regions, which agrees with previous observation of metal epitaxy on graphite surface<sup>S14</sup>. The high-nucleation-density areas on graphene can be linked to point and line defects, as indicated by STEM images in Fig. S7c and S7d, respectively. Au nanostructures on such defective regions usually appear as small and spherical particles surrounded by large nanoplatelets, which agrees with our hypothesis that friction of Au motion on freestanding Gr is negligible.

The correlation between surface contamination and formation of spherical Au nanostructures is further elaborated by comparing SEM images of the same graphene-covered hole in the Quantifoil grid before and after deposition of Au, as shown in Fig. S8. Our results indicate the cleanness of freestanding graphene is crucial for the observation of low-nucleation-density surface, in accordance with previous TEM studies of atomic-scale metal nucleation on graphene<sup>S15</sup>.

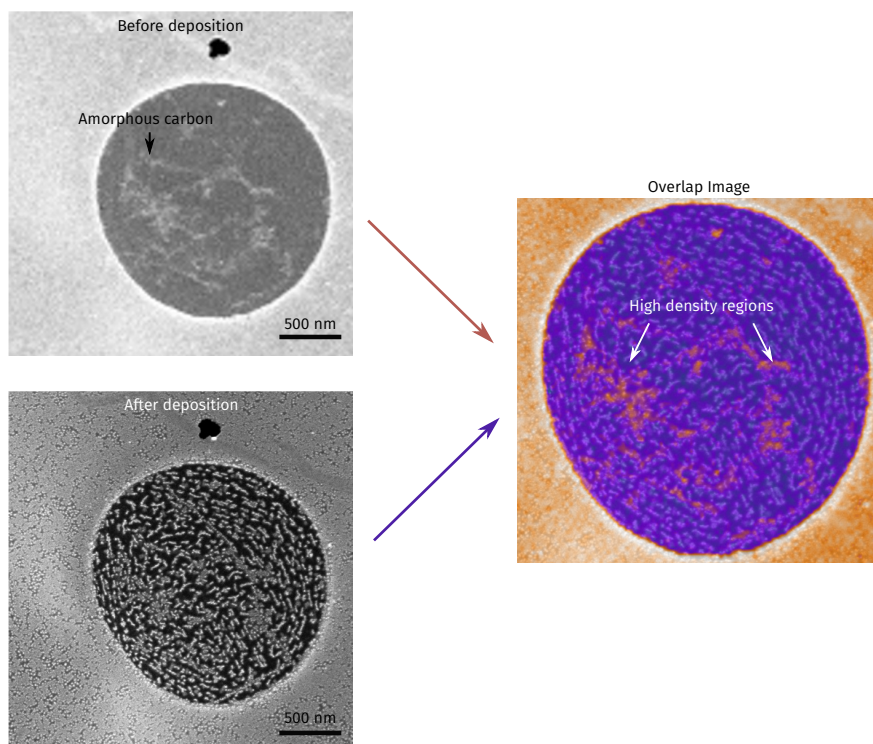


Figure S8: **Influence of surface contamination on the Au morphology on freestanding graphene.** SEM images show that the brighter regions corresponding to amorphous carbon contamination on freestanding graphene before deposition (top left panel) coincide with the areas of high nucleation density after deposition (bottom left panel), which is confirmed by superimposing the SEM images before and after deposition (right panel).

Unlike spherical clusters observed in a-C/Gr/Au system, Au platelets in Vac/Gr/Au usually appear more

regular geometries, such as hexagons or triangles. In addition to hexagonal Au platelets shown in Fig. 2d, Fig. S9 displays the STEM characteristics of a triangular Au platelet. From the FT-STEM image in Fig. S9b, in addition to the  $\{\frac{4}{3}\frac{2}{3}\frac{2}{3}\}$  (and its double-spacing counterpart  $\{\frac{2}{3}\frac{1}{3}\frac{1}{3}\}$ ) lattice planes, another set of  $\{200\}$  peaks emerges, corresponding to the  $\langle 001 \rangle$  zone axis perpendicular to the graphene surface. The co-existence of two sets of diffraction planes indicate the Au platelet is thicker than a few monolayers. Detailed topography profiles of these Au nanostructures were measured by atomic force microscopy (AFM) in section S2.2.

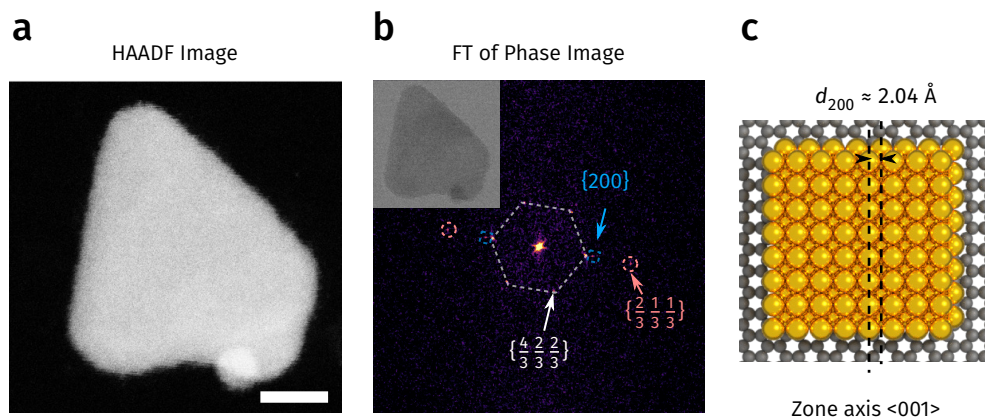


Figure S9: **Characterization of triangular Au nanostructures.** **a** STEM image of selected triangular Au nanostructure with high-angle annular dark field (HAADF) detector. Scale bar: 5 nm. **b** Fourier-transformed (FT) image of the phase signal (inset), showing mixed lattice plane sets corresponding to  $\{200\}$  (blue),  $\{\frac{4}{3}\frac{2}{3}\frac{2}{3}\}$  (white) and  $\{\frac{2}{3}\frac{1}{3}\frac{1}{3}\}$  (pink, double-spacing of  $\{\frac{4}{3}\frac{2}{3}\frac{2}{3}\}$ ) families. **c** Scheme of the  $(200)$  lattice plane seen from the  $\langle 001 \rangle$  zone axis of the face-center-cubic (fcc) bulk crystal of Au.

## S2.2 AFM characterizations

To investigate the mechanism of 2D Au nanoplatelets formation on freestanding graphene, we performed detailed analysis of their height and size distribution on different graphene surfaces using AFM. Freestanding graphene on perforated  $\text{SiN}_x$  chips were used for all AFM experiments to overcome the issue of high surface corrugation of amorphous carbon substrate after annealing. The  $\text{SiN}_x$  substrate surface remained flat after annealing. As shown in Fig. S10a, the freestanding graphene surface was highly corrugated, with height prominence at the order of 20 nm, which is corroborated by deformation mapping of the same area as shown in Fig. S10b. Despite the use of polymer coating during graphene transfer, the annealing process almost completely removed the PMMA residue, as indicated by the AFM topography in the inset of Fig. S10a.

Table S1 compares the root mean square (RMS) roughness  $R_q$  and arithmetic roughness  $R_a$  for as-prepared

freestanding and substrate-supported graphene surfaces. The roughness of freestanding graphene is significantly higher than that of substrate-supported graphene, indicating the observed low nucleation density on freestanding graphene is not caused by structural superlubricity<sup>S12,S16</sup> which were observed on ultraflat graphite surface.

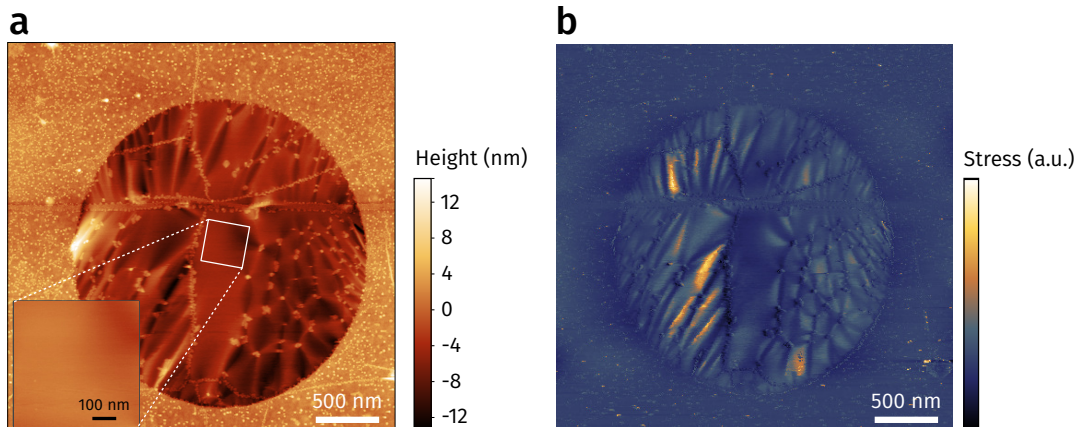


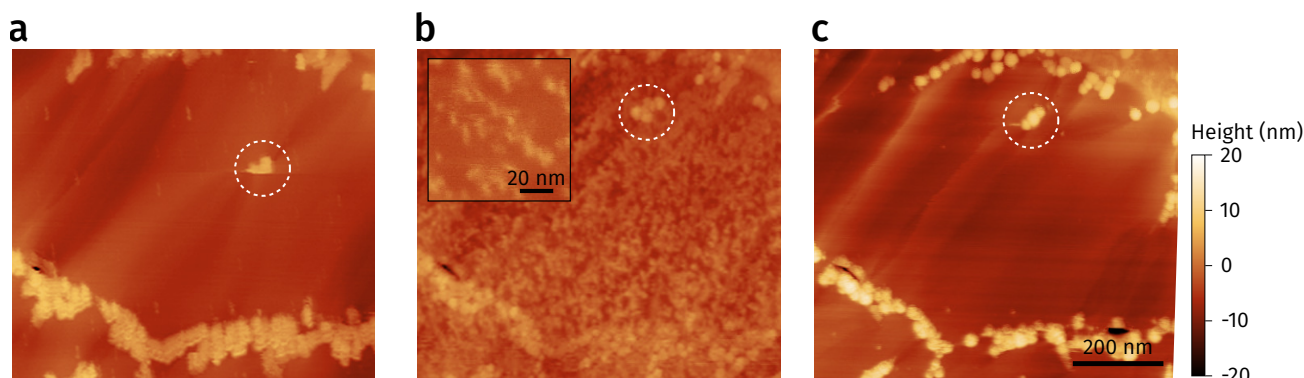
Figure S10: **AFM topographic and stress images of a graphene-covered hole in  $\text{SiN}_x$  substrate after Au deposition.** **a** and **b** show the same mapped area with height and deformation signals, respectively. Inset of **a** shows the topography on a non-wettable region on freestanding graphene (color scale normalized for visualization).

Table S1: **Root mean square (RMS) roughness  $R_q$  and arithmetic roughness  $R_a$  of different graphene surfaces after annealing.** The mean roughness of freestanding graphene is substantially higher than the substrate-supported graphene surfaces due to high degree of wrinkle and surface corrugation.

	Freestanding Gr	a-C/Gr	$\text{SiN}_x/\text{Gr}$	$\text{SiO}_2/\text{Gr}$
RMS Roughness $R_q$ (nm)	$2.15 \pm 0.61$	$0.663 \pm 0.029$	$0.409 \pm 0.042$	$0.242 \pm 0.019$
Arithmetic Roughness $R_a$ (nm)	$1.70 \pm 0.45$	$0.450 \pm 0.015$	$0.324 \pm 0.028$	$0.195 \pm 0.011$

Using AFM, we were also able to identify the influence of thermal annealing by comparing the topography of the same region before and after thermal treatment. Fig. S11a shows the AFM topography of Vac/Gr/Au directly after Au evaporation with large non-wettable area. However, after placing the sample under ambient conditions for 1 day, significant contamination layer with average height of  $1 \sim 2$  nm was observed on the previously clean regions (Fig. S11b and inset). Such airborne contaminants resembles those in a recent report<sup>S17</sup>, and their average height is distinguishable from the evaporated Au nanostructures. Interestingly, after re-annealing the sample under Ar/ $\text{H}_2$  environment, the contaminants completely removed (Fig. S11c). The comparison clearly indicates thermal annealing of graphene sample prior to the Au evaporation is the

key to obtain clean and non-wettable freestanding graphene surface, as the hydrocarbon contaminants are known to promote metal nucleation on graphitic surfaces<sup>S15,S18,S19</sup>. We also found that one Au particle on



**Figure S11: Effect of thermal annealing on the quality of freestanding graphene and Au nanostructure.**

**a** AFM topography of Vac/Gr/Au directly after Au deposition. **b** AFM topography of same area after the sample was kept in ambient for 24 hours. Airborne contamination can clearly be observed. Inset: zoomed-in mapping on the contaminated area. **c** The same area after re-annealing the sample at 600 °C. The amorphous contaminants were completely removed, while the average height of Au nanostructures increases. Note the Au nanostructure marked in white circle appeared to be moved from **a** to **c**.

the freestanding graphene surface (marked in white circle, Fig. S11a-c) had apparent lateral displacement before and after the thermal treatment. On the contrary, although the shape and height changed after thermal annealing, Au nanostructures near line defects and on SiN<sub>x</sub>/Gr surface showed negligible movement. We therefore conclude that on freestanding graphene, Au nanostructures with lateral length up to tens of nanometers could still have considerable high mobility and low friction.

The movement of Au nanostructures could also be induced by external mechanical force. As shown in Fig. S12, during continuous AFM scanning in ambient, the triangular Au platelet (marked in white dashed lines) showed significant lateral displacement (> 2 times of its size). However, such displacement was not observed for Au clusters evaporated on line defects or substrate-supported graphene. Consider the huge difference between the lateral size of Au platelet (> 50 nm) and the apex of AFM tip (ScanAsys Air, ~ 2 nm), it is unlikely that such displacement was caused by pickup and re-deposition by the AFM tip<sup>S20</sup>.

The tip-induced motion of Au platelets can be explained by the reduction of equilibrium Gr-Au interaction potential caused by the many-body repulsive interaction. Following our analysis in section S1.3, the attractive potential of Vac/Gr/Au system is significantly reduced compared with the Sub/Gr/Au system when  $d$  is close to the vdW contact distance (Fig. S3). Similarly, on defective area, we expect the attractive potential to be

also large due to the strong adhesion between defective graphene and Au<sup>S15</sup>. As a result, interaction between the AFM tip and the Au platelet on freestanding graphene can easily overcome the attractive potential between Au and graphene, leading to considerable lateral displacement.

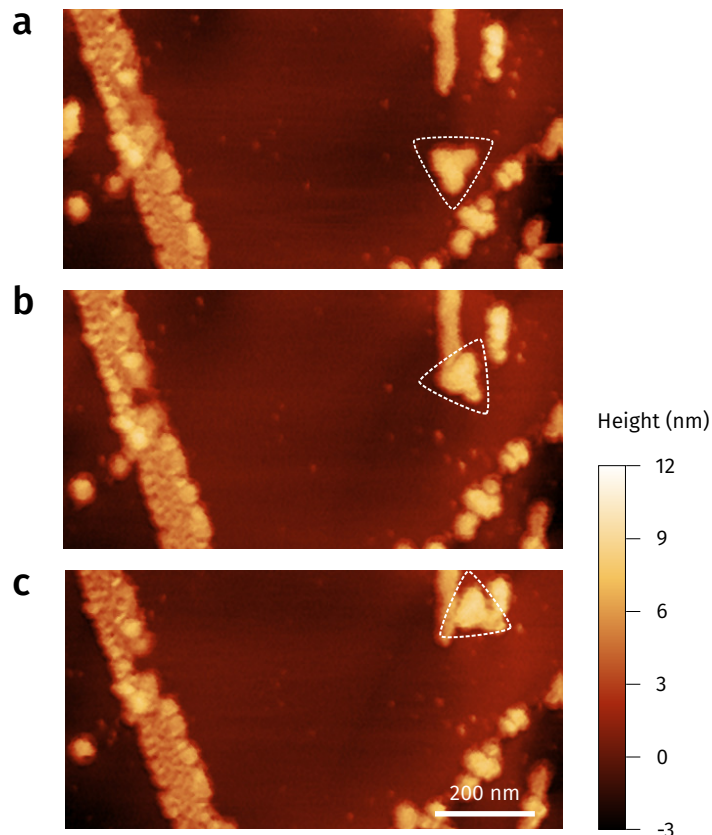


Figure S12: **Observation of Au nanostructure displacement during AFM measurement in ambient.** **a, b** and **c** are consecutive AFM images of Au nanostructure on freestanding graphene surface taken during continuous scanning. A triangular nanoplatelet on freestanding graphene appeared to move  $>200$  nm ( $>2$  times the lateral size of Au platelet) induced by the motion of AFM tip. On the other hand, no apparent change of morphology was observed for Au deposited on line defects. The results indicate that the friction between freestanding graphene and Au nanostructures with lateral size  $> 50$  nm is still considerably small.

### S2.3 Discussion about mechanism

More details about the mechanism of 2D Au platelets formation on freestanding graphene are discussed as follows. First we rule out the possibility that larger Au structure formation was due to that Au is easier to wet freestanding graphene. As shown in Fig. S13, if such thermodynamic hypothesis is correct, it is more energetically favorable for the Au clusters to be adsorbed on freestanding graphene than the separated

system. In other words,  $\Delta G_{\text{ad}} < \Delta G_{\text{sep}}$  is expected, where  $\Delta G_{\text{ad}}$  and  $\Delta G_{\text{sep}}$  are the free energy of adsorbed and separated systems, respectively. Assume the surface area of graphene is  $A_{\text{Gr}}$ , the surface area of isolated Au is  $A_{\text{Au}}$ , and the fraction of Au-covered graphene surface is  $f$ , we have:

$$\Delta G_{\text{sep}} = A_{\text{Gr}}\gamma_{\text{Gr}} + A_{\text{Au}}\gamma_{\text{Au}} + \Delta G_{\text{co}} \quad (\text{S9})$$

$$\Delta G_{\text{ad}} = A_{\text{Gr}}(1-f)\gamma_{\text{Gr}} + A_{\text{Gr}}f\gamma_{\text{Au-Gr}} + A_{\text{Gr}}f\gamma_{\text{Au}} + \Delta G_{\text{co}}$$

where  $\gamma_{\text{Au}}$  and  $\gamma_{\text{Gr}}$  are the surface energy of Au and freestanding graphene, respectively,  $\gamma_{\text{Au-Gr}}$  is the interfacial energy between Au and graphene, and  $\Delta G_{\text{co}}$  is the free energy of cohesion (chemical bonding). Consider the fact  $A_{\text{Gr}} \gg A_{\text{Au}}$ , the inequality  $\Delta G_{\text{ad}} < \Delta G_{\text{sep}}$  can be approximated by

$$\gamma_{\text{Au}} + \gamma_{\text{Au-Gr}} < \gamma_{\text{Gr}} \quad (\text{S10})$$

Since  $\gamma_{\text{Au}} \gg \gamma_{\text{Gr}}$ ,  $\gamma_{\text{Au-Gr}}$  must be negative. Combine with  $\gamma_{\text{Au-Gr}} = \gamma_{\text{Gr}} + \gamma_{\text{Au}} - \Delta W_{\text{Au-Gr}}$ , where  $\Delta W_{\text{Au-Gr}}$  is the work of adhesion between graphene and Au,  $\Delta W_{\text{Au-Gr}}$  should be considerably high to allow the wetting of Au on freestanding graphene to occur. This is nonphysical since i) attractive vdW potential is stronger with substrate-supported graphene, following the discussion in section S1.3 and ii) stronger adhesion leads to higher nucleation density, contradictory to our experimental findings.

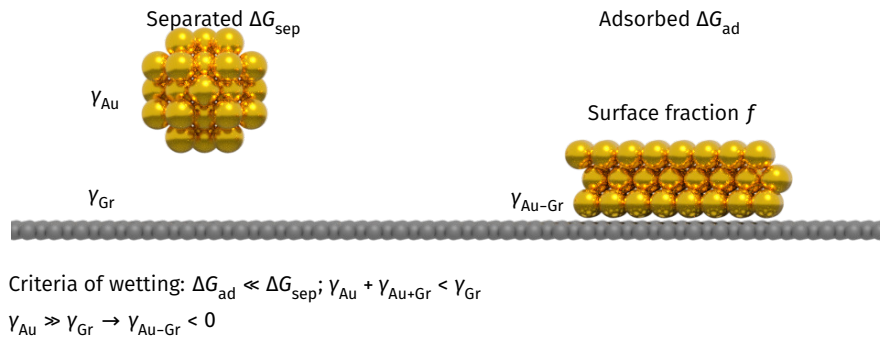


Figure S13: **Thermodynamic considerations of a 2D platelet formed on freestanding graphene.** Wetting of high-surface-energy Au on Gr indicates the free energy of adsorbed system  $\Delta G_{\text{ad}}$  should be smaller than in the separated system  $\Delta G_{\text{sep}}$ , which in turn means the interfacial tension  $\gamma_{\text{Au-Gr}}$  is negative and adhesion between Au and Gr increases. This contradicts to the experimental observation of ultra-low condensation of Au on freestanding graphene.

To further study the formation of large 2D platelets on freestanding graphene, we performed statistic analysis for the Au nanostructures grown on different graphene surfaces using both AFM topography and

SEM micrograph. As shown in Fig. S14, the Au nucleation density measured by AFM ranks  $\text{Vac/Gr} < \text{SiO}_2/\text{Gr} < \text{SiN}_x/\text{Gr} < \text{a-C/Gr}$ , which agrees with our SEM images in Fig. 2e. Fig. S14 compares the AFM height distribution of Au nanostructures from  $> 500$  samples points per graphene surface measured. The fitted distribution curves indicate that the height of Au nanostructures follows  $\text{Vac/Gr} > \text{SiO}_2/\text{Gr} \approx \text{SiN}_x/\text{Gr} > \text{a-C/Gr}$ . In other words,  $\text{Vac/Gr}$  is actually slightly *less wettable* to Au than the substrate-supported graphene surfaces, in particular  $\text{a-C/Gr}$ , which agrees with our analysis in Fig. S3. On the other hand, the average particle area for  $\text{Vac/Gr/Au}$  increases by  $> 10^2$  times compared with that for  $\text{a-C/Gr/Au}$ , as shown in Fig. S14c. Notably, the distribution of particle area for  $\text{Vac/Gr/Au}$  has an tail towards  $10^4 \text{ nm}^2$ . In combination with the observation of low friction interface between  $\text{Vac/Gr}$  and Au (Fig. S12), we conclude that the formation of larger 2D crystals on freestanding graphene, can only be ascribed to kinetic effects. In fact, such 2D platelet formation may be metastable, as we observed the height of Au nanostructures on freestanding graphene increased from  $\sim 6 \text{ nm}$  (as prepared, Fig. S11a) to  $\sim 14 \text{ nm}$  after annealing at  $600 \text{ }^\circ\text{C}$  (Fig. S11c), further proving that the freestanding graphene is poorly wettable by Au.

To estimate the surface diffusivity  $D$  of Au on different graphene surfaces, we compared the nucleation density  $N_{\text{nu}}$  measured by SEM images as shown in Fig. S15 insets. The ratios  $D_{\text{fs}}^*/D_{\text{i}}^*$  between the effective diffusivities on freestanding graphene ( $D_{\text{fs}}^*$ ) and graphene surface  $i$  ( $D_{\text{i}}^*$ ) calculated using the relation  $N_{\text{nu}} \propto (D^*)^{-1/3}$ , are also plotted. The effective diffusivity on freestanding graphene can be up to  $10^9$  times faster than that on  $\text{a-C/Gr}$ . Furthermore, although the average particle area on  $\text{Vac/Gr/Au}$  is larger than that of substrate-supported graphene, the low nucleation density leads to less amount of Au deposited on  $\text{Vac/Gr}$  surface, as a result of the existence of repulsive vdW interaction.

To rule out the possibility that the variation of Au nucleation density is influenced by the defects of the CVD-grown graphene, we also measured Au morphology on mechanically-exfoliated graphene. Monolayer (ML) graphene mechanically exfoliated onto  $\text{SiO}_2$  substrate was identified by optical micrograph (Fig. S16a). As shown in Fig. S16b-d, the nucleation density, morphology and height distributions of Au deposited onto mechanically-exfoliated graphene are similar to those observed in  $\text{SiO}_2/\text{Gr/Au}$  samples prepared using CVD-grown graphene.

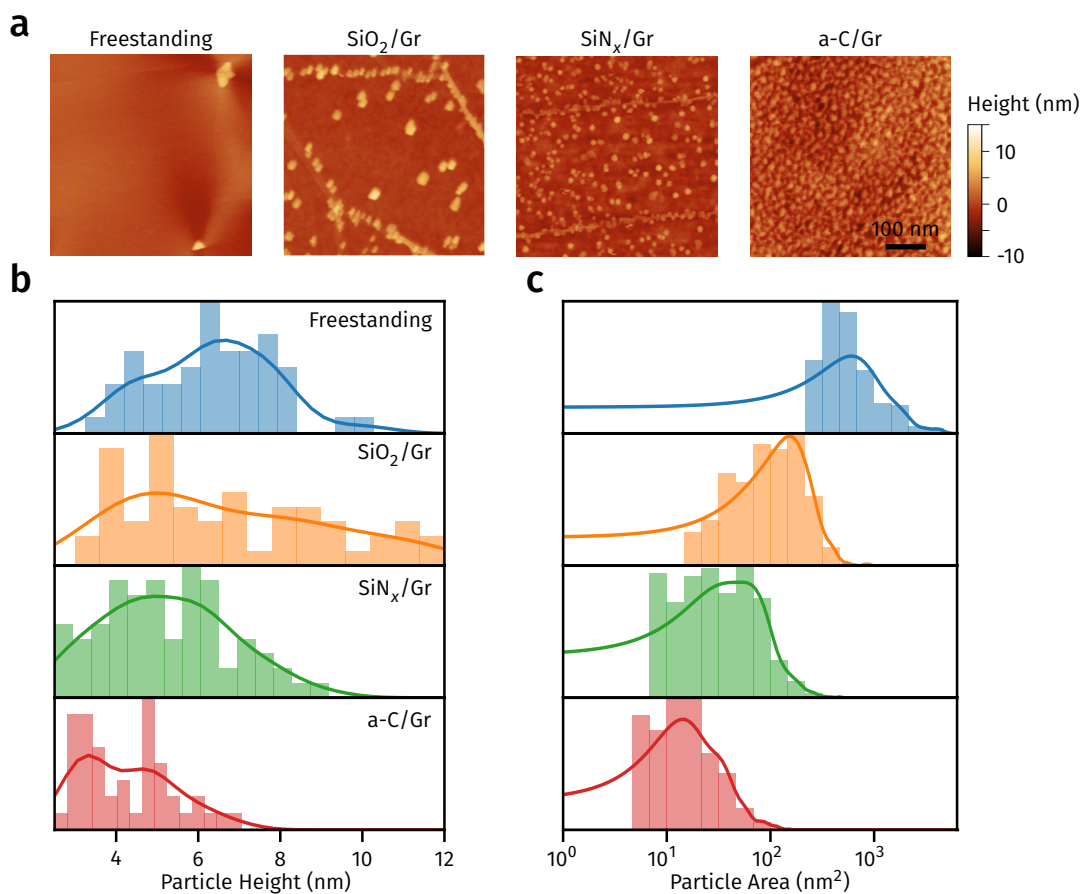


Figure S14: **Statistics of Au nanostructures grown on freestanding or substrate-supported graphene surfaces.** **a.** AFM topography of Au deposited on freestanding graphene and graphene supported by SiO<sub>2</sub>, SiN<sub>x</sub> and a-C substrates. **b** and **c.** Height and surface area distribution of Au particles on different graphene interfaces, respectively. The solid line in **b** and **c** are the continuous distribution function fitted using Gaussian kernel. Au nanoparticles on freestanding graphene are slightly higher while much larger in lateral size compared with those on substrate-supported graphene. The statistics were based on both AFM and SEM measurements.

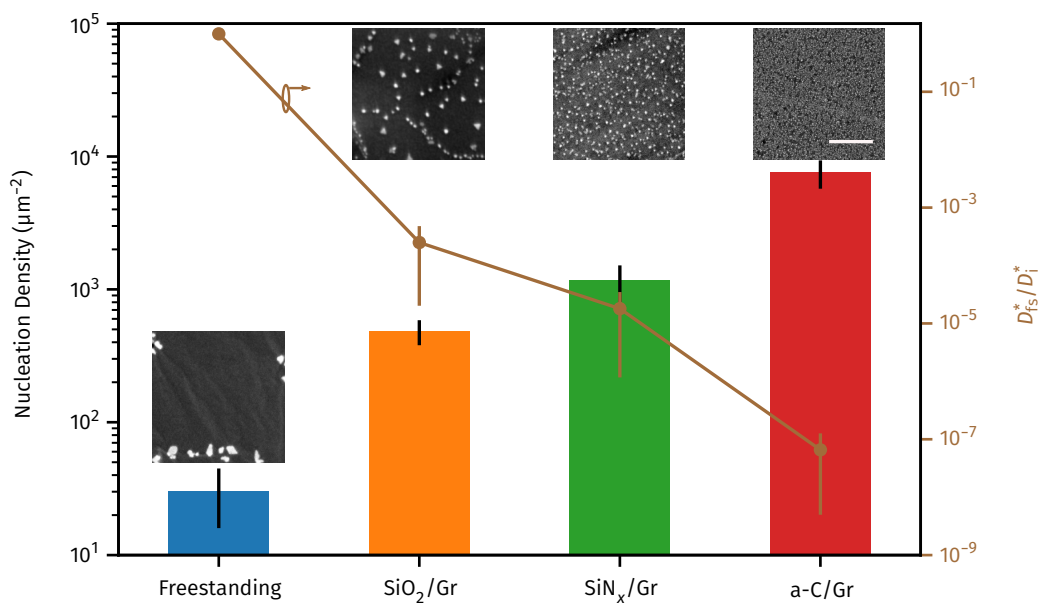
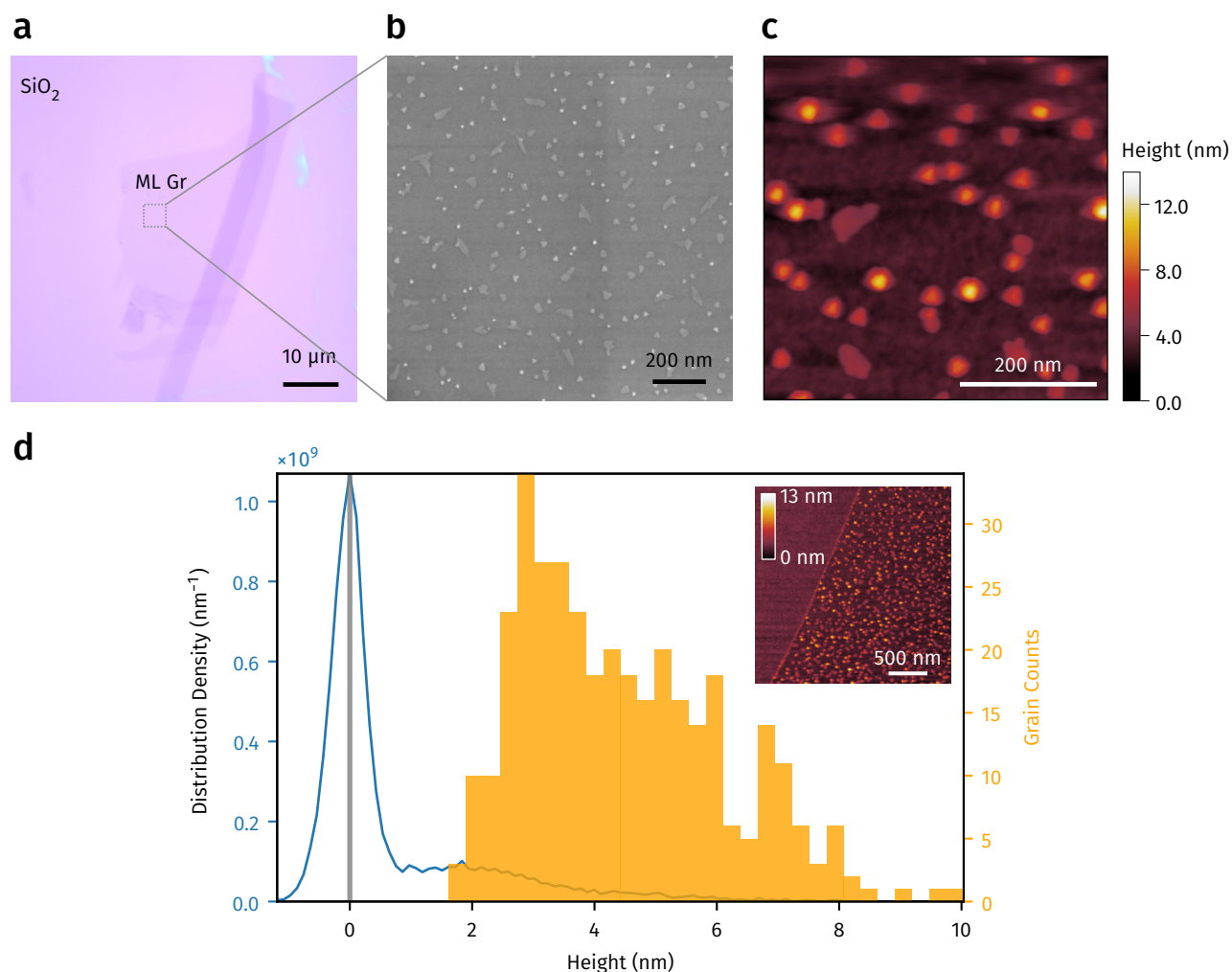


Figure S15: **Histograms of nucleation density (left vertical axis) and corresponding SEM images of Au morphology on graphene with different substrates.** The calculated ratio  $D_{fs}^*/D_i^*$  between effective surface diffusivities of freestanding graphene ( $D_{fs}^*$ ) and graphene supported by substrate  $i$  ( $D_i^*$ ) are shown as the right vertical axis. Scale bars of SEM insets: 200 nm.



**Figure S16: Au nanostructures deposited on mechanically-exfoliated substrate-supported graphene. a** Optical image of a piece of exfoliated graphene transferred onto  $\text{SiO}_2$  substrate. Monolayer (ML) regions are identified by optical contrast. **b** and **c** SEM and AFM characterizations of Au nanostructures on freestanding Gr when the nominal deposition thickness is 0.1 nm, respectively. Despite the clean graphene surface created by mechanical exfoliation, nucleation density of Au clusters is still higher than on freestanding Gr (Fig. 2d). **d.** Left axis: height distribution density of all pixels in the inset AFM image, the reference level of the substrate (0 nm) is taken as the center of the first peak. Right axis: histogram of average height per Au nanoplatelet in the inset AFM image, showing similar trend with Fig. S14c.

## S2.4 KMC simulations of Au diffusion

The detailed kinetic processes and their corresponding activation energy barriers in the KMC simulations are schematically shown in Fig. S17. The KMC simulation box was implemented on a  $m \times n \times 2$  triangular mesh with periodic boundary conditions (PBC), as shown in Fig. S18. To simulate the experimental conditions on the CVD-grown graphene, we implemented line and point defects on top of the triangular meshes (Fig. S18a, pink dots) by assigning higher diffusion barrier  $\Delta E_d^*$ . Practically, when simulating very fast Au diffusion on freestanding graphene, such defective regions act as preferential nucleation sites to promote growth of larger Au platelets. A typical snapshot of the KMC simulation can be seen in Fig. S18b.

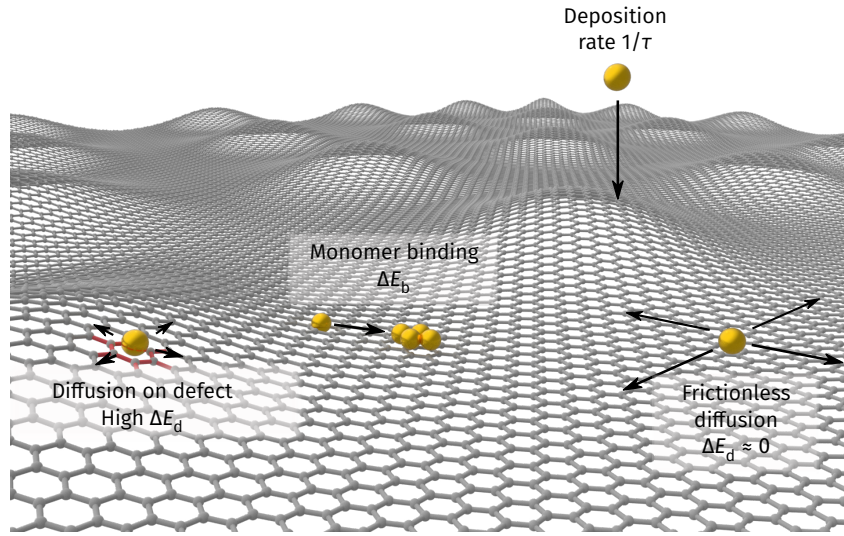


Figure S17: **Scheme of different kinetic processes for the Au deposited on freestanding Gr.** The Au atoms are deposited onto the freestanding Gr surface with a rate of  $1/\tau$ , where  $\tau$  is the characteristic time interval of incoming Au atoms. On pristine Gr interface, the diffusion energy barrier  $\Delta E_d$  is nearly negligible, leading to friction-less diffusion, while on defective / contaminated area  $\Delta E_d$  is much higher. On the other hand, Au atoms are bonded to form covalent structures with a energy barrier of  $\Delta E_b$ . The formation of large 2D Au structures are enabled when  $\Delta E_d$  on pristine freestanding Gr is even much lower than  $\Delta E_b$ .

The Au evaporation process is modeled as follows. The rate of deposition is defined as  $\nu = 1/\tau$ , where  $\tau$  is the characteristic time scale between two deposition events, which follows:

$$\nu = J_e N_{\text{site}} = \nu_0 \exp\left(-\frac{\Delta E_e}{k_B T}\right) \quad (\text{S11})$$

where  $J_e$  is the flux of evaporation (measured in  $\text{ML}\cdot\text{s}^{-1}$ ),  $N_{\text{site}}$  is the density of lattice sites in the KMC

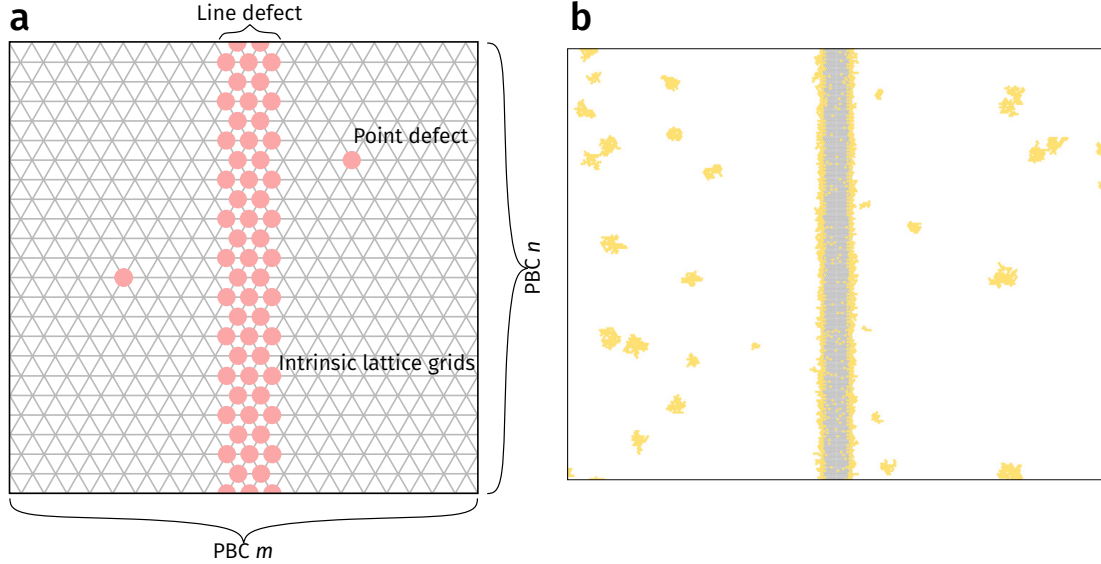


Figure S18: **Schematic diagram of simulation box used in our 2D lattice-KMC.** **a** The simulation box consists of  $m \times n \times 2$  triangle grids on which Au atoms are allowed to move. Line and point defects (pink dots) are implemented by assigning higher  $\Delta E_d$  value onto corresponding grid points. **b** Snapshot of a KMC simulation containing line defects. Yellow dots represents Au.

simulation,  $\nu_0$  is the rate prefactor, and  $\Delta E_e$  is the effective energy barrier for the evaporation process. For  $J_e = 0.01 \text{ ML}\cdot\text{s}^{-1}$ ,  $m = n = 100$  and  $\nu_0 = 10^{10} \text{ s}^{-1}$ , we have  $\Delta E_e \approx 15k_B T$ . We also note in the current KMC framework, the difference between freestanding and substrate-supported graphene is reflected by the choice of  $\Delta E_d^0$ , and surface corrugation is not taken into account.

There are several simplifications used in the KMC simulations. First, we do not specify whether the Au on each mesh grid is a single atom or a cluster. As a result, the binding between two Au units may be slower than that of surface diffusion. To simplify the simulation, the Au units are not allowed to move after coalescence occurs. Moreover, since in this study we do not care about absolute time scale of cluster formation, the exact value for  $\nu_0$  does not affect the final result.

The morphology of Au nanostructures are majorly influenced by the following factors: i) magnitude of  $\Delta E_e$  and ii) competition between  $\Delta E_d$  and  $\Delta E_b$ . For all simulations we fix the diffusion barrier on defects  $\Delta E_d^*$  to  $15 k_B T$ .

**Influence of  $\Delta E_e$**  Fig. S19 compares the different snapshots of Au nanostructures by varying  $\Delta E_e$  (horizontal direction) and  $\Delta E_d^0$  (vertical direction). Independent of the in-plane diffusion rate, by lowering  $\Delta E_e$  (faster deposition), the nucleation density of Au nanostructures always increases. This is because when in-

creasing the evaporation rate, there are more mobile Au on the graphene surface at the same time, leading to higher rate of coalescence. In the experiment of Au evaporation, it is therefore always favorable to use lower deposition rate for the formation of sparse and large clusters on freestanding graphene.

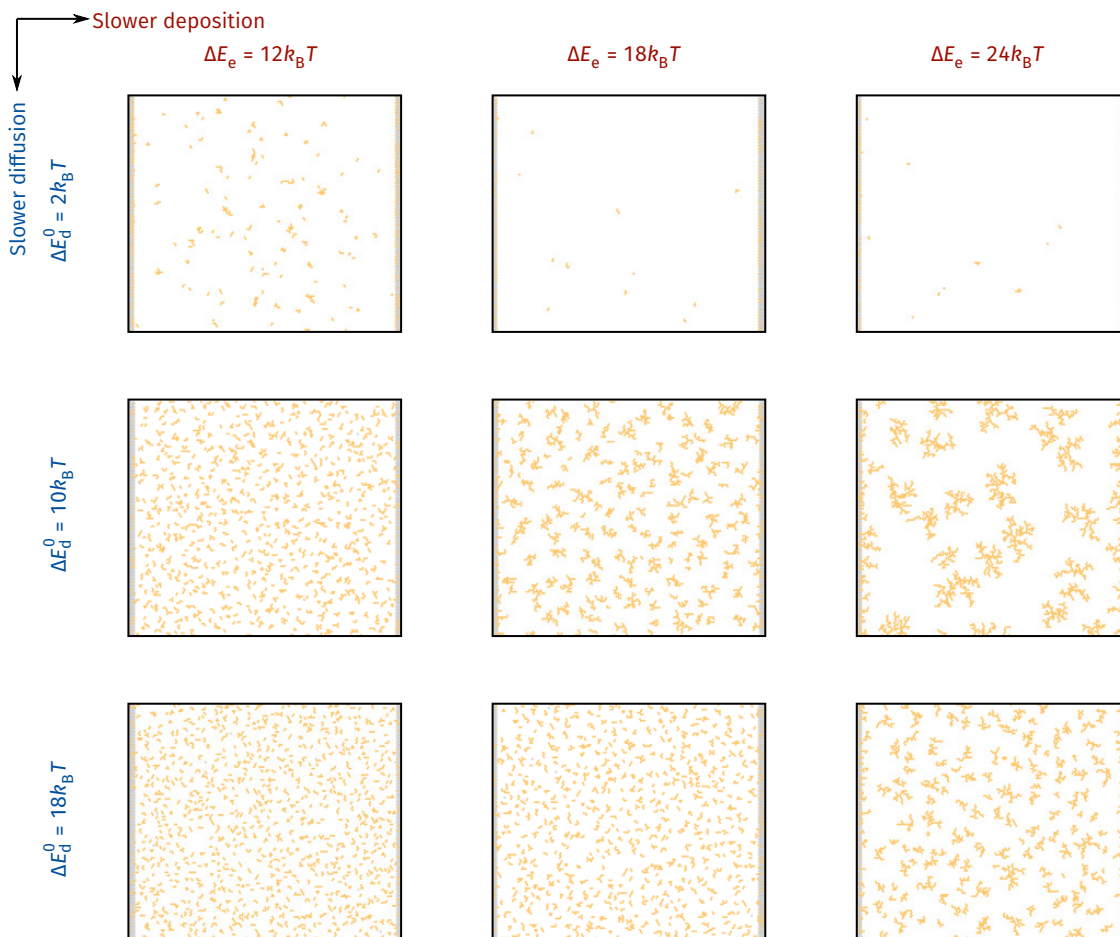


Figure S19: **Snapshots of Au nanostructure formation at  $10^6$  time steps by varying  $\Delta E_e$  and  $\Delta E_d^0$ .** Independent of  $\Delta E_d^0$ , decreasing  $\Delta E_e$  always leads to higher nucleation density. The value of  $\Delta E_b$  is  $10k_B T$  for all simulations. The line defects are plot at the edge of the simulation box for illustration purpose. Note for very fast diffusion cases, the time scale of individual cluster to grow appears to be longer than  $10^6$  steps, leading to smaller cluster size.

**Influence of  $\Delta E_d^0$  and  $\Delta E_b$**  The influence of  $\Delta E_d^0$  and  $\Delta E_b$  on the Au nanostructure formation is more complex. As shown in Fig. S20, with a lower  $\Delta E_d^0/\Delta E_b$  ratio, the nucleation density of Au nanostructures decreases. On the other hand, we also observe that at same  $\Delta E_d^0/\Delta E_b$  ratio, increasing  $\Delta E_d^0$  leads to formation of higher degree of nucleation. In both scenarios, the increasing of nucleation density can be explained

by shorter time scale for Au coalescence to occur.

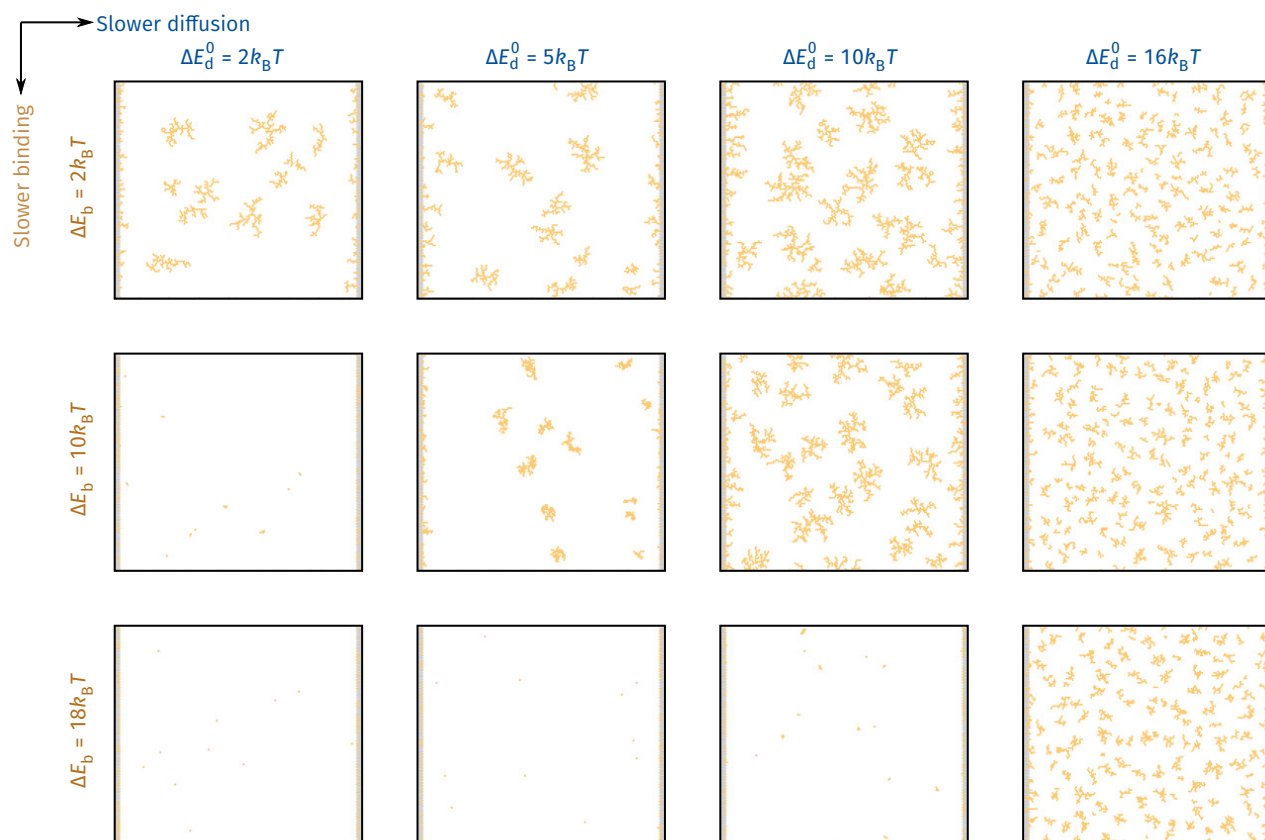


Figure S20: **Snapshots of Au nanostructure formation at  $10^6$  time steps by varying  $\Delta E_b$  and  $\Delta E_d^0$ .** Different  $\Delta E_b^0/\Delta E_d$  ratios lead to distinct morphology and nucleation density of Au nanostructures. The value of  $\Delta E_c$  is  $20k_B T$  for all simulations. The line defects are plot at the edge of the simulation box for illustration purpose. Note for very fast diffusion cases, the time scale of individual cluster to grow appears to be longer than  $10^6$  steps, leading to smaller cluster size.

The  $\Delta E_d^0/\Delta E_b$  ratio also influences the morphology of individual Au nanostructure. A general trend observed in Fig. S20 is that for higher  $\Delta E_d^0/\Delta E_b$  value, the Au nanostructure tends to dendritic, while for lower  $\Delta E_d^0/\Delta E_b$  value the Au nanostructures becomes more compact. This can be explained by the fact that when the rate of binding and diffusion are comparable, the structure formed is not fully relaxed. We use this feature to explain the distinct Au morphology observed on bulk graphite and freestanding graphene surfaces, as shown in Fig. S21. Although the nucleation density of Graphite/Au (Fig. S21a) at room temperature is comparable with that of Vac/Graphene/au (Fig. S21b), the dendritic pattern formation on Graphite/Au indicates the in-plane diffusion of Au is faster on freestanding graphene, given the fact that the Au-Au coalescence rate is almost independent on the substrate<sup>S21,S22</sup>. On the other hand, previous studies showed

that hexagonal/triangular Au nanostructures on graphite could only be formed during high-temperature deposition<sup>S13,S18,S19</sup>, indicating that  $\Delta E_d^0$  on freestanding graphene is lower than of bulk graphite. Taking the surface corrugation of freestanding graphene into account, the fast in-plane Au diffusion on freestanding graphene beyond the structural superlubricity, can only be explained by the existence of manybody repulsive vdW interactions.

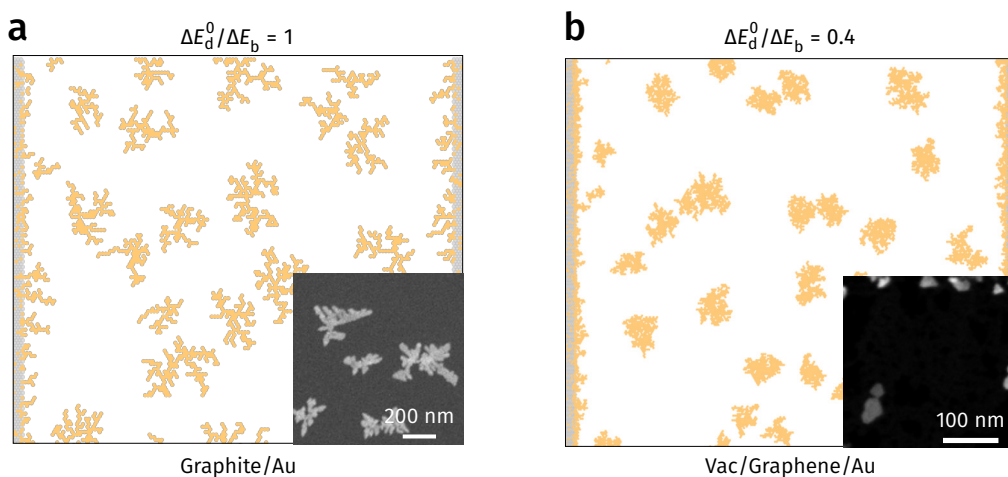


Figure S21: **Simulated morphology of Au nanostructures on bulk graphite (a) and freestanding graphene (b) surfaces.** The dendritic patterns on graphite are formed as a result of the high  $\Delta E_d^0/\Delta E_b$  ratio, while hexagonal and triangular structures are observed on freestanding graphene due to lower  $\Delta E_d^0/\Delta E_b$ . Experimental SEM images for Graphite/Au and Vac/Graphene/Au fabricated from Au evaporation at room temperature are shown as insets of **a** and **b**, respectively.

### S3 Molecular epitaxy of BPE molecules

#### S3.1 Practical considerations

Molecular epitaxy on graphene surface is known to be influenced by the doping state of graphene<sup>S23</sup>. To rule out the possibility that observed polymorphism of BPE was due to doping, Raman spectroscopy was used to monitor the charge density of graphene transferred on as-cleaned SiO<sub>2</sub> (SiO<sub>2</sub>/Gr), self-assembled octadecyltrichlorosilane (OTS) on SiO<sub>2</sub> (OTS/Gr) and gold (Au/Gr). The OTS-SiO<sub>2</sub> substrate was used as a reference for suppressing potential substrate-induced doping<sup>S24</sup>. As shown in Fig. S22, on all substrates the 2D peak is higher than the G peak, and D peak intensity is negligible. As summarized in Table S2, the 2D and G peak positions of SiO<sub>2</sub>/Gr and Au/Gr samples are statistically similar. From literature<sup>S25</sup>, the positions

of the G-peak for SiO<sub>2</sub>/Gr and Au/Gr indicates both samples have doping density less than  $2 \times 10^{12} \text{ e}\cdot\text{cm}^{-2}$ .

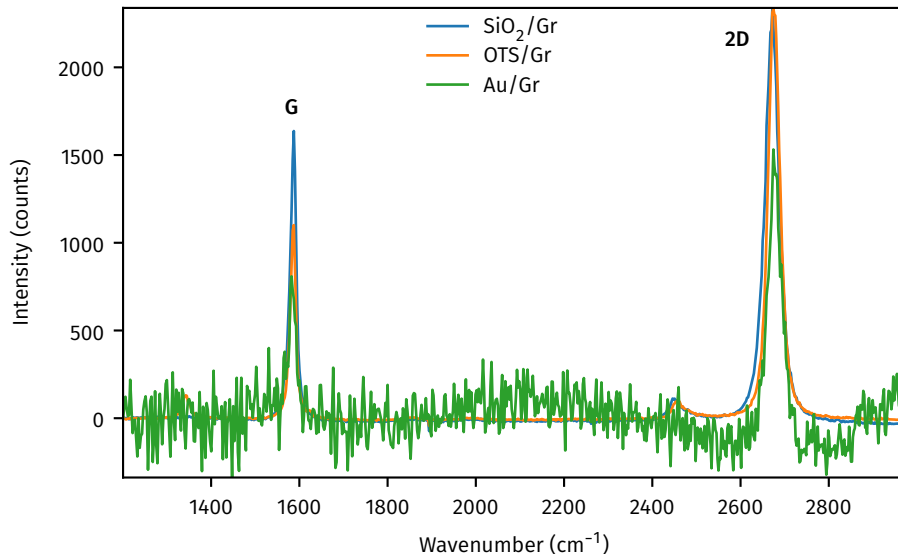


Figure S22: **Typical Raman spectra of monolayer graphene transferred onto as-cleaned SiO<sub>2</sub> (SiO<sub>2</sub>/Gr), OTS-treated SiO<sub>2</sub> (OTS/Gr) and gold (Au/Gr) substrates.** Raman spectra were taken using 532 nm laser. In all cases the 2D peak remains higher than G peak indicating monolayer graphene. The positions of 2D and G peaks do not have apparent shift, similar doping densities in these substrates.

Table S2: **Peak position and full width at half-maximum (FWHM) of G and 2D peaks in the Raman spectra in Fig. S22.** Statistical average and deviation are taken from over 80 data points. The peak parameters are fitted using Gaussian function.

Substrate	Position G (cm <sup>-1</sup> )	FWHM G (cm <sup>-1</sup> )	Position 2D (cm <sup>-1</sup> )	FWHM 2D (cm <sup>-1</sup> )
SiO <sub>2</sub> /Gr	1585.69/2.69	8.33/2.30	2675.62/4.15	17.75/2.52
OTS/Gr	1584.76/1.07	8.07/1.48	2676.42/2.57	16.05/3.16
Au/Gr	1582.50/2.48	10.31/2.93	2676.25/3.43	18.80/2.05

### S3.2 Determining crystallographic parameters

The processes for determining the crystallographic parameters (crystal lattice constant and interplanar distances) are described as follows. The full-range GIWAXS spectra for SiO<sub>2</sub>/Gr/BPE and Au/Gr/BPE are shown in Fig. S23. A rectangular beam stop was used to reduced the scattering from the substrate. The 1D diffraction profile was generated by first subtracting the background from the 2D GIWAXS spectra using

rolling-ball algorithm<sup>S26</sup>, and calculated using:

$$I_{1D}(q) = \int_0^{\pi/2} I_{2D}(q, \theta) q d\theta \quad (\text{S12})$$

where  $I_{2D}$  and  $I_{1D}$  are the 2D and 1D X-ray diffraction intensity,  $q = |\mathbf{q}|$  is magnitude of the diffraction wave vector, and  $\theta = \arctan \left| \frac{q_z}{q_{xy}} \right|$ .

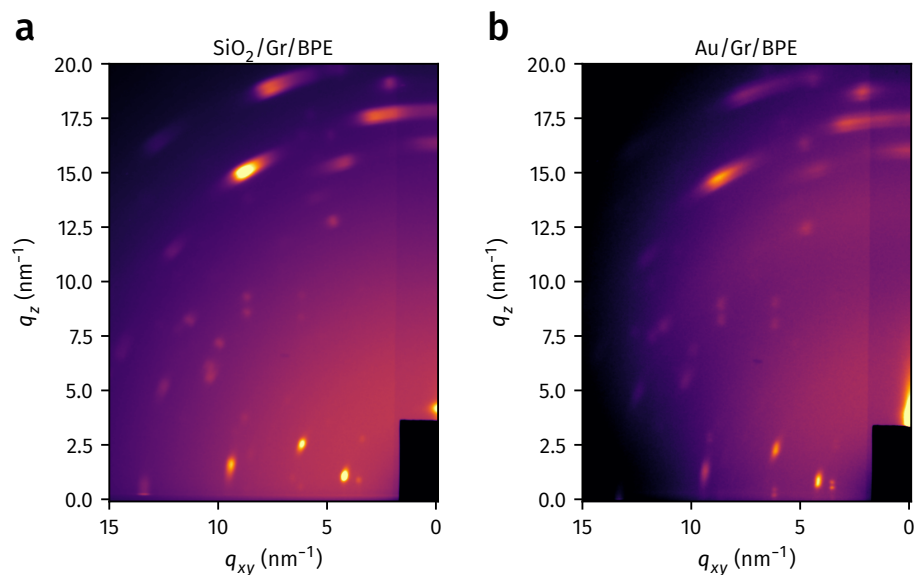


Figure S23: Full-range GIWAXS spectra of SiO<sub>2</sub>/Gr/BPE (a) and Au/Gr/BPE (b) systems corresponding to Fig. 3c

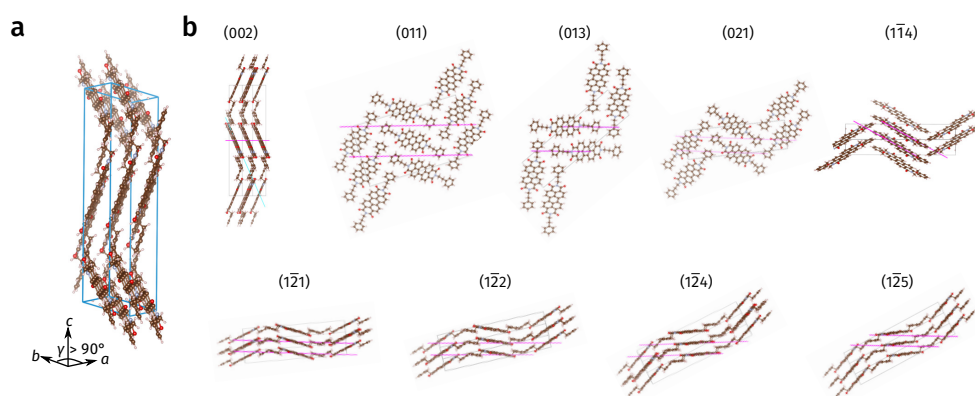


Figure S24: **Lattice structure of BPE.** **a.** Schematic of BPE unit cell with monoclinic symmetry. **b.** Typical lattice planes in BPE single crystal with corresponding  $(hkl)$  indices.

Single crystal data of BPE molecule from literature<sup>S27</sup> (CCDC DICNIM01) were used as a reference for assigning the Miller indices for the lattice planes. As shown in Fig. S24a, the unit cell of BPE single crystal is

monoclinic with  $\gamma \neq 90^\circ$ . The major diffraction planes are shown in Fig. S24b. The high- $q$  (short interplanar distance) diffraction planes ( $1\bar{1}4$ ), ( $1\bar{2}1$ ), ( $1\bar{2}2$ ), ( $1\bar{2}4$ ) and ( $1\bar{2}5$ ) are associated with the PTCDI basal plane of BPE molecule. The simulated 1D X-ray diffraction profile from BPE single crystal data is shown in Fig. S25 (black line). In comparison, Fig. S25 also show the experimental 1D X-ray diffraction profiles for sublimed BPE powder (blue line), SiO<sub>2</sub>/Gr/BPE (orange line) and Au/Gr/BPE (green line). The diffraction peaks in the experimental 1D X-ray diffraction profiles were assigned as follows. Assuming the BPE molecules in the experimental samples remained the monoclinic lattice structure, we first guessed the Miller indices for the most prominent peaks in each 1D profile using the reference data from BPE single crystal. The lattice constants  $a$ ,  $b$ ,  $c$ ,  $\gamma$  were then calculated using least-square fitting based on the equation of interplanar spacing in a monoclinic unit cell<sup>S28</sup>:

$$\frac{1}{d_{hkl}^2} = \frac{1}{\sin^2 \gamma} \left[ \frac{h^2}{a^2} + \frac{k^2}{b^2} + \frac{l^2 \sin^2 \gamma}{c^2} - \frac{2hk \cos \gamma}{ab} \right] \quad (\text{S13})$$

where  $d_{hkl} = 2\pi(q_{hkl})^{-1}$  is the interplanar distance. The assignment of Miller indices was refined iteratively until the mismatches between experimental and the fitted values  $d_{hkl}$  were minimized. The peak assignment for BPE powder, SiO<sub>2</sub>/Gr/BPE and Au/Gr/BPE are labeled in Fig. S25, with the fitted lattice constants and  $q_{hkl}$  values listed in Tables S3 and S4, respectively. Comparing with BPE powder, SiO<sub>2</sub>/Gr/BPE and Au/Gr/BPE show expansion in  $b$ -axis and shrinking in  $c$ -axis, possibly due to the templating effect of graphene<sup>S23</sup>. We find that the best-fitted lattice constants  $b$  and  $c$  for Au/Gr/BPE has about 1% expansion compared with that for SiO<sub>2</sub>/Gr/BPE, corresponding to the increasing of interplanar distance between the PTCDI basal planes in Au/Gr/BPE.

Table S3: **Best fitted Lattice constants for BPE single crystal<sup>S27</sup>, BPE powder sample, SiO<sub>2</sub>/Gr/BPE and Au/Gr/BPE using monoclinic lattice model.**

	$a$ (Å)	$b$ (Å)	$c$ (Å)	$\gamma$ (°)
BPE single crystal <sup>S27</sup>	4.73	9.51	32.45	100.27
BPE powder	4.64±0.03	9.34±0.04	31.09±0.08	99.71±0.84
SiO <sub>2</sub> /Gr/BPE	5.01±0.08	9.56±0.03	29.94±0.16	99.76±0.85
Au/Gr/BPE	4.87±0.09	9.67±0.04	30.29±0.27	100.28±1.03

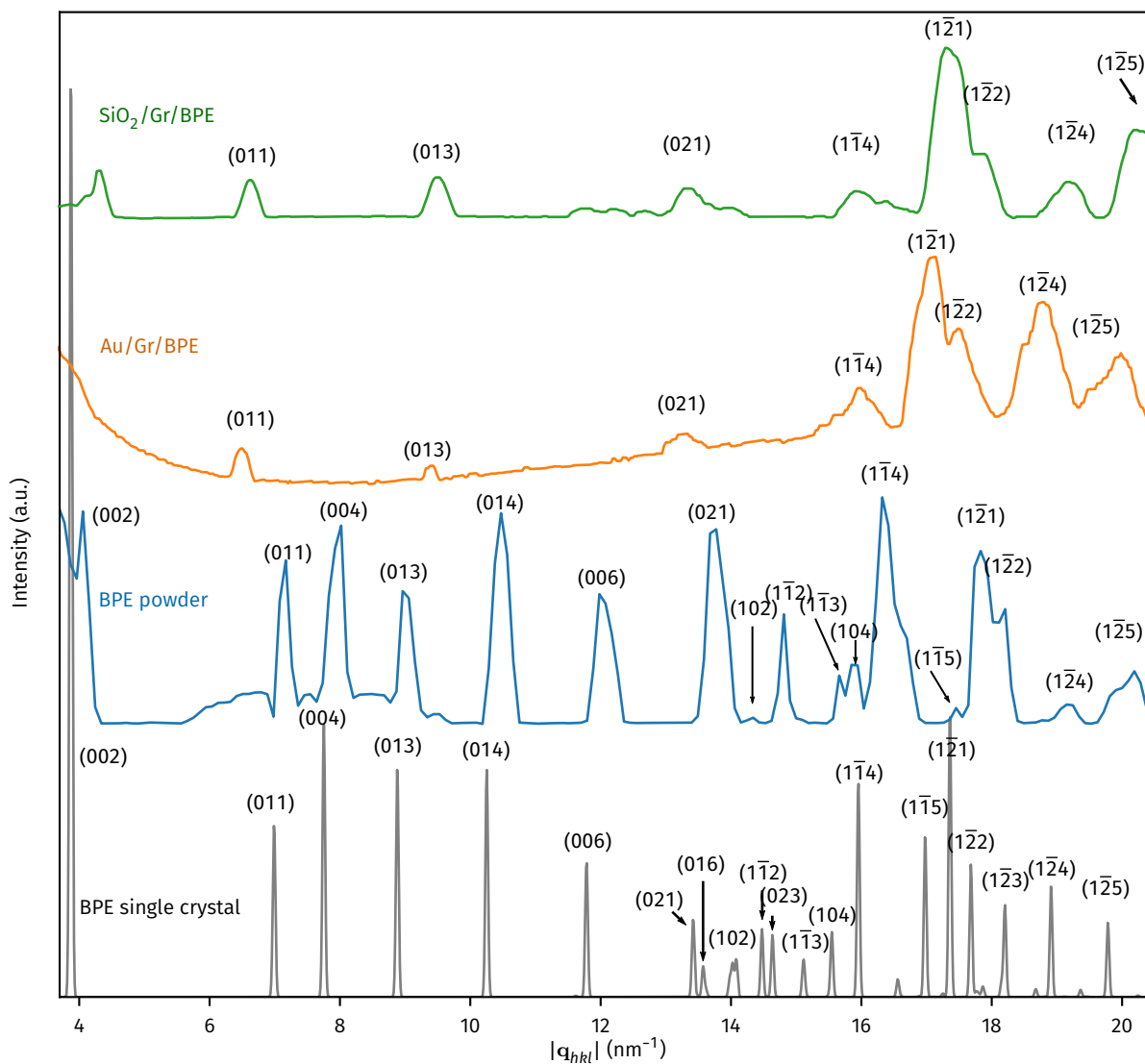


Figure S25: **1D X-ray diffraction patterns of BPE single crystal, BPE powder, SiO<sub>2</sub>/Gr/BPE and Au/Gr/BPE.** The best-fitted (*hkl*) indices are labeled. Diffraction of BPE single crystal is simulated using the RIETAN-FP package within the VESTA software<sup>S29</sup>.

Table S4: **Best fitted  $|q_{hkl}|$  values of major Bragg diffraction peaks ( $hkl$ ) for BPE single crystal<sup>S27</sup>, BPE powder, SiO<sub>2</sub>/Gr/BPE and Au/Gr/BPE using monoclinic lattice model.** Blank fields indicate the corresponding diffraction peaks are weak in the sample.

$(hkl)$	$ q_{hkl} $ (nm <sup>-1</sup> )			
	BPE single crystal <sup>S27</sup>	BPE powder	SiO <sub>2</sub> /Gr/BPE	Au/Gr/BPE
(002)	3.87	4.04		
(011)	6.99	7.12	7.26	7.00
(004)	7.75	8.09		
(013)	8.88	9.13	9.38	9.13
(014)	10.25	10.58		
(006)	11.62	12.13		
(021)	13.57	13.80	13.61	13.37
(102)	14.03	14.32		
( $\bar{1}$ 12)	14.48	14.83		
( $\bar{1}$ 13)	15.11	15.51		
(104)	15.55	15.94		
( $\bar{1}$ 14)	15.95	16.40	16.02	15.99
( $\bar{1}$ 15)	16.98	17.49		
( $\bar{1}$ 21)	17.36	17.77	17.47	17.14
( $\bar{1}$ 22)	17.68	18.11	17.84	17.51
( $\bar{1}$ 24)	18.91	19.42	19.27	18.82
( $\bar{1}$ 25)	19.78	20.34	20.27	19.93

### S3.3 Breakdown of wetting transparency theory

An important evidence supporting the existence of repulsive vdW interaction in Au/Gr/BPE system is the breakdown of wetting transparency theory as observed from the lattice packing of BPE molecules on bare substrates. From the Lifshitz theory, the magnitude of attractive vdW interaction between substrate and BPE layer over vacuum monotonically increases when the dielectric responses of the substrate become stronger. Therefore, when BPE molecules are evaporated on Au surface (Au/Vac/BPE), the vdW interaction potential becomes more negative compared with the SiO<sub>2</sub>/Vac/BPE system, as shown in Fig. S26.

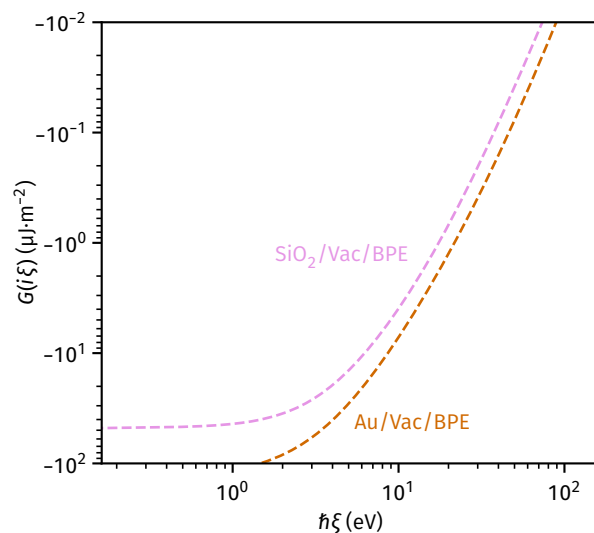


Figure S26: **Single-frequency interaction energy  $G(i\xi)$  as function for  $\hbar\xi$  of BPE/Vac/SiO<sub>2</sub> (violet) and BPE/Vac/Au systems.** In contrast to the  $G(i\xi)$  of graphene-mediated systems in Fig. 3b, the interaction between BPE and bare Au substrate is significantly stronger (more negative interaction potential) than that on bare SiO<sub>2</sub> substrate over the entire frequency range.

The change of substrate-BPE interaction leads to significant difference of BPE orientation between SiO<sub>2</sub>/Vac/BPE and Au/Vac/BPE as measured from 2D GIWAXS spectra. The diffraction plane corresponding to the strongest Laue spot changes from (002) in SiO<sub>2</sub>/Vac/BPE (Fig. S27a and S27c) to (013) in Au/Vac/BPE (Fig. S27b and S27d). The PTCDI planes are brought closer to the Au surface due to the stronger Au-BPE interaction compared with that on the SiO<sub>2</sub>-BPE interface.

The classical wetting transparency theory for 2D materials<sup>S7,S8</sup> clearly breaks down for the systems studied here. From the wetting transparency theory based on additive model of vdW interactions, stronger interactions between Au-BPE over vacuum will also lead to stronger vdW interactions in Au/Gr/BPE. Our observation of lattice expansion in Au/Gr/BPE clearly cannot be captured by classical wetting transparency theory.

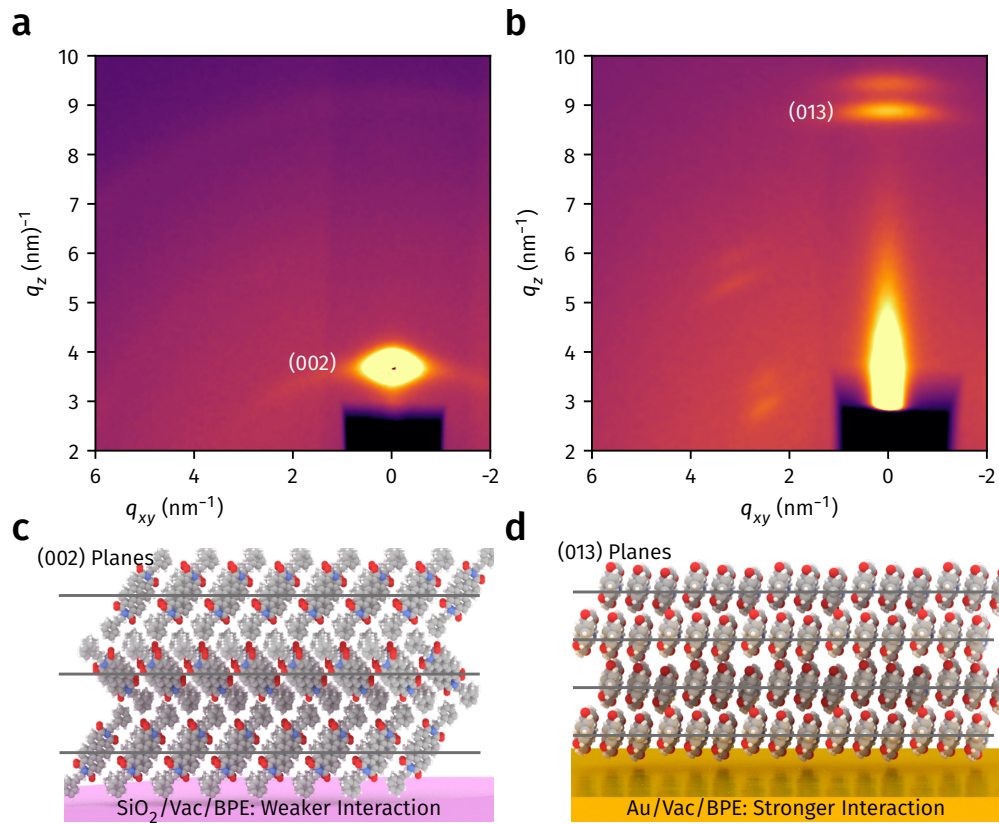


Figure S27: **GIWAXS spectra of BPE deposited on bare SiO<sub>2</sub> (a) and Au (b) substrates.** The principal peaks in BPE/Gr/SiO<sub>2</sub> and BPE/Gr/Au are (002) and (013) lattice planes, respectively. The larger distance of (002) compared with (013) lattice plane agrees with the stronger interaction in BPE/Vac/Au configuration. **c** and **d** Schemes of (002) and (013) lattice planes corresponding to **a** and **b**, respectively.

## References

- S1. Li, J.-L. *et al.* Use of dielectric functions in the theory of dispersion forces. *Phys. Rev. B* **71**, 235412 (2005).
- S2. Parsegian, V. A. *Van der Waals Forces: A Handbook for Biologists, Chemists, Engineers, and Physicists* Cambridge Core. (2017).
- S3. Meurk, A., Luckham, P. F. & Bergström, L. Direct Measurement of Repulsive and Attractive van der Waals Forces between Inorganic Materials. *Langmuir* **13**, 3896–3899 (1997).
- S4. Munday, J. N., Capasso, F. & Parsegian, V. A. Measured long-range repulsive Casimir–Lifshitz forces. *Nature* **457**, 170–173 (2009).
- S5. Zhou, Y., Pellouchoud, L. A. & Reed, E. J. The potential for fast van der Waals computations for layered materials using a Lifshitz model. *2D Mater.* **4**, 025005 (2017).
- S6. Zhou, Y. & Reed, E. J. Microscopic Origins of the Variability of Water Contact Angle with Adsorbed Contaminants on Layered Materials. *J. Phys. Chem. C* **122**, 18520–18527 (2018).
- S7. Rafiee, J. *et al.* Wetting transparency of graphene. *Nat. Mater.* **11**, 217–222 (2012).
- S8. Shih, C.-J. *et al.* Breakdown in the Wetting Transparency of Graphene. *Phys. Rev. Lett.* **109**, 176101 (2012).
- S9. Celebi, K. *et al.* Ultimate Permeation Across Atomically Thin Porous Graphene. *Science* **344**, 289–292 (2014).
- S10. Liang, X. *et al.* Toward Clean and Crackless Transfer of Graphene. *ACS Nano* **5**, 9144–9153 (2011).
- S11. Lin, Y.-C. *et al.* Graphene Annealing: How Clean Can It Be? *Nano Lett.* **12**, 414–419 (2011).
- S12. Cihan, E., İpek, S., Durgun, E. & Baykara, M. Z. Structural lubricity under ambient conditions. *Nat. Commun.* **7**, 12055 (2016).
- S13. Cihan, E., Özoğul, A. & Baykara, M. Z. Structure and nanotribology of thermally deposited gold nanoparticles on graphite. *Appl. Surf. Sci.* **354**, 429–436 (2015).
- S14. Cross, C. E., Hemminger, J. C. & Penner, R. M. Physical Vapor Deposition of One-Dimensional Nanoparticle Arrays on Graphite: Seeding the Electrodeposition of Gold Nanowires. *Langmuir* **23**, 10372–10379 (2007).

- S15. Zan, R., Bangert, U., Ramasse, Q. & Novoselov, K. S. Evolution of Gold Nanostructures on Graphene. *Small* **7**, 2868–2872 (2011).
- S16. Özoğul, A., İpek, S., Durgun, E. & Baykara, M. Z. Structural superlubricity of platinum on graphite under ambient conditions: The effects of chemistry and geometry. *Appl. Phys. Lett.* **111**, 211602 (2017).
- S17. Temiryazev, A., Frolov, A. & Temiryazeva, M. Atomic-force microscopy study of self-assembled atmospheric contamination on graphene and graphite surfaces. *Carbon* **143**, 30–37 (2019).
- S18. Wayman, C. & Darby, T. Nucleation and growth of gold films on graphite. *J. Cryst. Growth* **28**, 53–67 (1975).
- S19. Darby, T. & Wayman, C. Nucleation and growth of gold films on graphite. *J. Cryst. Growth* **28**, 41–52 (1975).
- S20. Hsieh, S. *et al.* Imaging and Manipulation of Gold Nanorods with an Atomic Force Microscope. *J. Phys. Chem. B* **106**, 231–234 (2002).
- S21. Lewis, L. J., Jensen, P., Combe, N. & Barrat, J.-L. Diffusion of gold nanoclusters on graphite. *Phys. Rev. B* **61**, 16084–16090 (2000).
- S22. Bardotti, L. *et al.* Diffusion and aggregation of large antimony and gold clusters deposited on graphite. *Surf. Sci.* **367**, 276–292 (1996).
- S23. Tian, T. & Shih, C.-J. Molecular Epitaxy on Two-Dimensional Materials: The Interplay between Interactions. *Ind. Eng. Chem. Res.* **56**, 10552–10581 (2017).
- S24. Yan, Z. *et al.* Controlled Modulation of Electronic Properties of Graphene by Self-Assembled Monolayers on SiO<sub>2</sub> Substrates. *ACS Nano* **5**, 1535–1540 (2011).
- S25. Das, A. *et al.* Monitoring dopants by Raman scattering in an electrochemically top-gated graphene transistor. *Nat. Nanotechnol.* **3**, 210–215 (2008).
- S26. Schindelin, J. *et al.* Fiji: an open-source platform for biological-image analysis. *Nat. Methods* **9**, 676–682 (2012).
- S27. Mizuguchi, J. N,N'-Bis(2-phenethyl)perylene-3,4:9,10-bis(dicarboximide). *Acta Cryst. C* **54**, 1479–1481 (1998).

- S28. Andrews, K. W., Dyson, D. J. & Keown, S. R. *Interpretation of Electron Diffraction Patterns* (Springer, 1967).
- S29. Momma, K. & Izumi, F. VESTA: a three-dimensional visualization system for electronic and structural analysis. *J. Appl. Cryst.* **41**, 653–658 (2008).